IMMUNOLOGY

Elevated type I interferon responses potentiate metabolic dysfunction, inflammation, and accelerated aging in mtDNA mutator mice

Yuanjiu Lei[1], Camila Guerra Martinez[1], Sylvia Torres-Odio[1], Samantha L. Bell[1], Christine E. Birdwell[1], Joshua D. Bryant[1], Carl W. Tong[2], Robert O. Watson[1], Laura Ciaccia West[1], A. Phillip West[1]*

Mitochondrial dysfunction is a key driver of inflammatory responses in human disease. However, it remains unclear whether alterations in mitochondria-innate immune cross-talk contribute to the pathobiology of mitochondrial disorders and aging. Using the polymerase gamma (POLG) mutator model of mitochondrial DNA instability, we report that aberrant activation of the type I interferon (IFN-I) innate immune axis potentiates immunometabolic dysfunction, reduces health span, and accelerates aging in mutator mice. Mechanistically, elevated IFN-I signaling suppresses activation of nuclear factor erythroid 2–related factor 2 (NRF2), which increases oxidative stress, enhances proinflammatory cytokine responses, and accelerates metabolic dysfunction. Ablation of IFN-I signaling attenuates hyperinflammatory phenotypes by restoring NRF2 activity and reducing aerobic glycolysis, which combine to lessen cardiovascular and myeloid dysfunction in aged mutator mice. These findings further advance our knowledge of how mitochondrial dysfunction shapes innate immune responses and provide a framework for understanding mitochondria-driven immunopathology in POLG-related disorders and aging.

INTRODUCTION

An expanding body of literature indicates that mitochondria are key regulators of the mammalian innate immune response, with both beneficial and deleterious consequences for the host (*1*). Mitochondria serve as antiviral signaling hubs and facilitate antibacterial immunity by generating reactive oxygen species (ROS), but they can also promote inflammation following cellular damage and stress (*2*–*5*). Recent work has demonstrated that mitochondrial DNA (mtDNA) is a potent agonist of nucleic acid sensors of the innate immune system, including Toll-like receptor 9 (TLR9), NOD-like receptor family pyrin domain containing 3 (NLRP3), and cyclic GMP-AMP synthase (cGAS) (*6*, *7*). The cGAS-stimulator of interferon genes (STING) axis is now recognized as a major driver of type I interferon (IFN-I) and inflammatory responses to nuclear and mitochondrial genome instability, and the aberrant release of mtDNA from damaged cells and tissues is increasingly linked to a growing list of human diseases (*6*, *8*–*10*).

Mitochondrial diseases (MD) are a group of clinically heterogeneous disorders caused by inherited mutations in genes that function in oxidative phosphorylation (OXPHOS) and mitochondrial metabolism (*11*, *12*). In addition to exhibiting metabolic and energetic deficits, patients with MD are more susceptible to opportunistic pathogens and also suffer elevated complications arising from these infections (*13*–*15*). Although B and T cell immunodeficiencies can contribute to recurrent infections in MD (*16*), comparatively little is known about innate immune dysregulation in patients and/or murine models. Hyperactivation of the innate immune system is a key feature of sepsis, systemic inflammatory response syndrome (SIRS), and acute respiratory distress syndrome, all of which occur more frequently in patients with MD (*14*, *15*). Given the established and emerging links between mitochondria and innate immunity, persistent mitochondrial dysfunction in MD could basally activate or rewire the innate immune system. This could occur as loss of mitochondrial integrity and/or quality control liberates mitochondrial damage-associated molecular patterns, such as mtDNA, which engage the innate immune signaling and promote inflammatory responses that synergize with metabolic impairments to drive pathology. Accordingly, elevated inflammatory cytokines have been observed in patients with Alpers-Huttenlocher syndrome and mouse models of primary mitochondrial disorders, suggestive of heightened innate immune activation (*17*, *18*).

The mitochondrial polymerase gamma (POLG) enzyme has DNA polymerase and 3′ → 5′ DNA exonuclease activities, and nearly 250 pathogenic mutations in *POLG* have been linked to diseases including primary MD, parkinsonism, and cancer (*19*–*22*). Mutations in *POLG* represent the most prevalent single-gene cause of MD and are implicated in a range of disorders including Alpers-Huttenlocher syndrome, ataxia neuropathy spectrum, and progressive external ophthalmoplegia, all of which are characterized by multiple organ pathology with varying degrees of nervous, muscular, digestive, and endocrine system involvement. In recent years, several mouse models of POLG-related disease have been reported, the most well studied of which is the POLG mutator mouse (*23*, *24*). These knock-in mice contain D257A substitutions in the exonuclease domain, and animals homozygous for the mutant alleles exhibit disrupted exonuclease function and elevated mtDNA instability (i.e., accumulation of mtDNA point mutations, linear fragments, and deletions) (*25*). Because of the continued accumulation of mutations over time and the variability of mtDNA instability across cells and tissues (*26*), POLG mutator mice are not considered a bona fide model of any particular human MD. However, these animals present pathology that mirrors aspects of human MDs, including cardiomyopathy, progressive anemia, and sensorineural hearing

[1]Department of Microbial Pathogenesis and Immunology, College of Medicine, Texas A&M University, Bryan, TX, USA. [2]Department of Medical Physiology, College of Medicine, Texas A&M University, Bryan, TX, USA.
*Corresponding author. Email: awest@tamu.edu

loss. POLG mutator mice also display premature aging between 6 and 9 months, characterized by alopecia, osteoporosis, kyphosis, and decreased body weight, and consequently die between 13 and 15 months of age (*23*, *24*, *27*). Mitochondrial dysfunction and inflammation are key features of aging (*28*), yet whether the innate immune system contributes to POLG-related disease phenotypes and premature aging of mutator mice is unknown.

Here, we report that mutator mice exhibit a hyperinflammatory innate immune status that is driven by chronic engagement of the cGAS-STING–IFN-I axis. Persistent IFN-I signaling represses nuclear factor erythroid 2-related factor 2 (NRF2) activity, which increases oxidative stress and aerobic glycolysis that potentiate inflammation and age-related pathology in these animals. Our findings indicate that IFN-I signaling is a key driver of innate immune rewiring and multiorgan pathology in mutator mice and provide a strong rationale for more broadly examining IFN-I dysregulation in mitochondrial disorders and aging.

RESULTS

Innate immune hyperresponsiveness of POLG mutator mice is regulated by monocyte and neutrophil expansion

To begin to characterize innate immune alterations in the POLG mutator model of mtDNA disease, we used a lipopolysaccharide (LPS)–induced endotoxemia model and monitored circulating cytokines and survival after challenge. Both 6- and 12-month-old mutator cohorts succumbed faster to intraperitoneal LPS challenge (Fig. 1A and fig. S1C). In line with a more rapid mortality rate, we detected elevated levels of proinflammatory cytokines, chemokines, and IFN-Is in the plasma of LPS-challenged mutator mice at all ages compared to wild-type (WT) littermates (Fig. 1B and fig. S1, A and B), consistent with a prior report (*29*).

As circulating leukocyte populations are key mediators of the cytokine storm that contributes to endotoxin shock, we next examined the blood cell composition of 12-month-old cohorts. Although aged mutator mice exhibited B and T cell lymphopenia (fig. S1, D and E) (*30*, *31*), we noted a substantial expansion of innate immune cell types, namely, monocyte ($CD11b^+Ly6C^{hi}$) and neutrophil ($CD11b^+Ly6G^+$) populations, by flow cytometry (Fig. 1, C to F). We also observed increases in steady-state tumor necrosis factor–α (TNFα) and monocyte chemoattractant protein 1 (MCP-1/CCL2) in the plasma of aged mutators (fig. S1F). To next identify the sources of TNFα at baseline and after challenge, we used intracellular staining and multiparameter flow cytometry. B and T cell populations in mutator mice did not express higher levels of intracellular TNFα before or after ex vivo LPS stimulation (fig. S1G). However, $CD11b^+$ cells expressed more TNFα and interleukin-6 (IL-6) after challenge (Fig. 1, G and J, and fig. S1H). Quantitation across multiple experiments revealed that $CD11b^+Ly6C^{hi}$ inflammatory monocytes in mutator blood had the greatest intracellular TNFα intensity, both at rest and after LPS stimulation (Fig. 1, G to I). Although $CD11b^+Ly6G^+$ neutrophils were also more numerous in the mutator blood, their TNFα intensity was roughly 100-fold lower (Fig. 1, J to L), indicating that inflammatory monocyte expansion is most likely responsible for the elevated levels of plasma cytokines at rest and after TLR4 engagement. Similar expansion and elevated TNFα positivity were observed in monocyte and neutrophil lineage cells in the bone marrow of mutator mice (fig. S1, I and J). Last, oral infection of 9- to 10-month-old cohorts with *Listeria monocytogenes* resulted in notably higher proinflammatory cytokine levels in mutator plasma at day 3 (fig. S1K) but less bacterial dissemination to the spleen and liver at day 5 after infection (fig. S1L). These results are consistent with prior findings that $Ly6C^{hi}$ inflammatory monocytes predominantly control oral *Listeria* infection (*32*) and, together, suggest that $CD11b^+$ myeloid cell expansion and innate immune reprogramming drive systemic hyperinflammatory responses in mutator mice.

STING regulates enhanced IFN-I and proinflammatory responses in POLG mutator macrophages

To define the underlying signaling pathways that shape innate immune hyperresponsiveness in mutator mice, we performed RNA sequencing (RNA-seq) analysis of primary bone marrow–derived macrophages (BMDMs) and peritoneal macrophages (PerMacs) at rest and after LPS challenge. Pathway analysis of RNA-seq datasets revealed notable elevations in IFN/IFN regulatory factor (IRF), Janus kinase (JAK)/signal transducers and activators of transcription (STAT), and nuclear factor κB (NF-κB) signaling, as well as increased glycolytic metabolism and reactive oxygen and nitrogen species production in mutator macrophages (fig. S2A). Gene expression profiling of mutator macrophages revealed an enrichment of IFN-stimulated genes (ISGs) (Fig. 2, A and B), which was confirmed by quantitative reverse transcription polymerase chain reaction (qRT-PCR) analyses (Fig. 2, C and D, and fig. S2, B and C). Mutator macrophages also displayed augmented *Tnfa* and *Il1b* RNA (Fig. 2, E and F), as well as TNFα and IL-6 protein levels (Fig. 2, G and H), agreeing with the intracellular cytometry data of Fig. 1. Moreover, mutator macrophages produced higher levels of nitrite after LPS and IFNγ costimulation data (Fig. 2I), confirming pathway analysis of RNA-seq data. Last, IFN stimulatory DNA (ISD) transfection to directly engage cGAS-STING revealed elevated ISG and proinflammatory cytokine expression in mutator BMDMs (Fig. 2J), demonstrating that POLG mutator macrophages are broadly hyperresponsive to multiple innate immune stimuli.

STING is a key mediator of IFN-I and proinflammatory responses induced by cytosolic and extracellular mtDNA (*6*, *7*), and ablation of STING can limit mtDNA-driven inflammation in mouse models of acute kidney injury and Parkinson's disease (*33*–*35*). We observed that aged POLG mutator mice have markedly more circulating, cell-free mtDNA in the plasma, and we also noted that LPS-challenged mutator BMDMs liberate more mtDNA into the culture medium (fig. S2, D and E). We therefore reasoned that mtDNA instability and release in POLG mutator macrophages might drive constitutive IFN-I via the cGAS-STING pathway, leading to elevated proinflammatory responses after LPS. Notably, we observed that macrophages from POLG mutators crossed onto a STING-deficient background had lower ISG expression (fig. S2, F and G), as well as lower TNFα secretion (fig. S2H), when compared to STING-sufficient mutators. Together, our data suggest that mtDNA instability and release in POLG mutators engage STING, which potentiates macrophage activation to subsequent innate immune challenge.

The cGAS-STING–IFN-I signaling axis regulates monocyte and neutrophil expansion and hyperinflammatory responses in mutator mice

The early, inflammatory phase of septic shock is characterized by leukocyte activation and secretion of proinflammatory cytokines such as TNFα, IL-6, and IL-1β (*36*). IFN-I can exacerbate inflammation

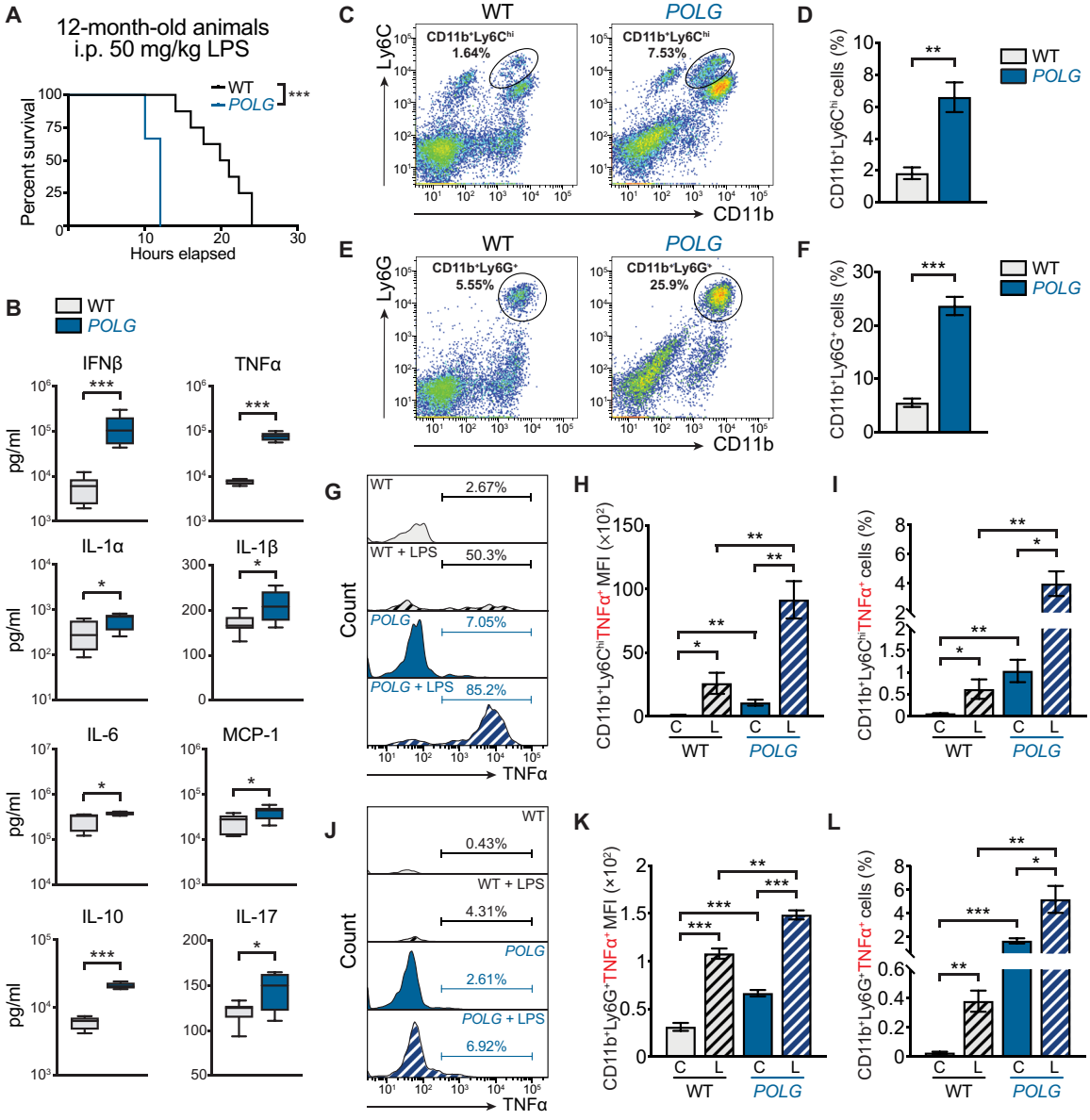

Fig. 1. POLG mutator mice exhibit a hyperinflammatory phenotype to LPS challenge due to increased CD11b$^+$ myeloid cells in the blood. (**A** and **B**) Twelve-month-old WT ($n = 8$) and POLG ($n = 7$) mice were challenged with LPS [50 mg/kg by intraperitoneal (i.p.) injection]. Kaplan-Meyer survival analysis was performed (A). Plasma cytokine profiles were determined by multianalyte bead-based immunoassay on $n \geq 6$ biological samples per group (B). Log-rank (Mantel-Cox) test was used to compare percent survival between different groups. (**C** and **D**) CD11b$^+$Ly6C^{hi} inflammatory monocyte population in whole blood from 12-month-old WT and POLG mice was evaluated by flow cytometry. Pseudo-color plots are representative of four independent experiments (C), and quantification of the percentage of CD11b$^+$Ly6C^{hi} cells is shown in (D). (**E** and **F**) CD11b$^+$Ly6G$^+$ blood neutrophil population in 12-month-old WT and POLG mice was determined by flow cytometry. Pseudo-color plots are representative of four independent experiments (E), and quantification of the percentage of CD11b$^+$Ly6G$^+$ cells is shown in (F). (**G** to **I**) CD11b$^+$Ly6C^{hi}TNFα$^+$ inflammatory monocyte population in unstimulated (C) or LPS-challenged (L) whole blood from 12-month-old WT and POLG mice was evaluated by flow cytometry. Histograms are representative of four independent experiments (G). Quantification of CD11b$^+$Ly6C^{hi}TNFα$^+$ mean fluorescent intensity (MFI) is shown in (H), and the percentage of CD11b$^+$Ly6C^{hi}TNFα$^+$ cells is shown in (I). (**J** to **L**) CD11b$^+$Ly6G$^+$TNFα$^+$ neutrophil population in unstimulated or LPS-challenged whole blood from 12-month-old WT and POLG mice was evaluated by flow cytometry. Histograms are representative of four independent experiments (J). Quantification of CD11b$^+$Ly6G$^+$TNFα$^+$ MFI is shown in (K), and the percentage of CD11b$^+$Ly6G$^+$TNFα$^+$ neutrophils is shown in (L). Unless stated, statistical significance was determined using unpaired Student's t test after Shapiro-Wilk normality test. *$P < 0.05$, **$P < 0.01$, and ***$P < 0.001$. Error bars represent SEM.

in response to TNFα (*37*) and contributes to mortality in LPS-induced sepsis (*38*). Because we noted increased IFN-I secretion after LPS challenge (Fig. 1B) and more mtDNA was present in the plasma of aged POLG mutators (fig. S2D), we explored whether cGAS-STING signaling contributes to increased mortality after intraperitoneal LPS challenge. We observed delayed LPS-induced mortality (Fig. 3A) and markedly lower plasma cytokine levels in mutator mice lacking cGAS or STING (Fig. 3B). In line with a role for IFN-I signaling in

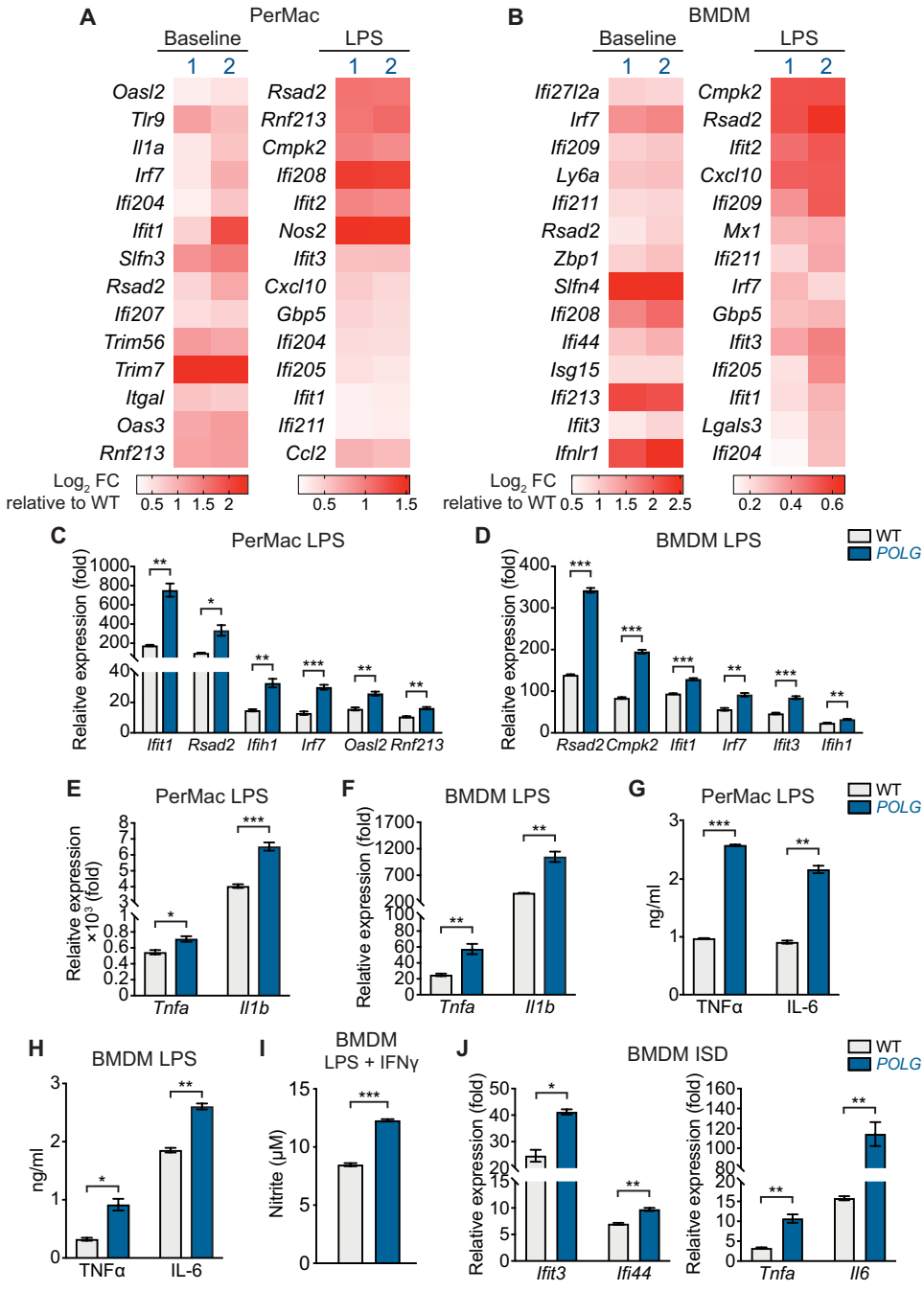

Fig. 2. POLG mutator macrophages exhibit enhanced IFN-I and proinflammatory responses after innate immune stimulation. (**A** and **B**) Heatmaps of RNA-seq data displaying most up-regulated ISGs in POLG mutator PerMacs (A) and BMDMs (B) at baseline and after LPS challenge (200 ng/ml for 6 hours). Log_2 fold changes (Log_2 FC) are relative to WT controls. (**C** to **F**) qRT-PCR analysis of ISG and proinflammatory cytokine expression in WT and POLG PerMacs (C and E) and BMDM (D and F) after 4 or 6 hours of LPS stimulation. (**G** and **H**) Proinflammatory cytokine secretion in WT and POLG PerMacs (G) or BMDMs (H) after 4 hours of LPS stimulation (20 ng/ml). (**I**) Nitrite levels in WT and POLG BMDM after 17 hours of LPS (20 ng/ml) + IFNγ (50 ng/ml) treatment. (**J**) qRT-PCR analysis of ISGs and cytokine expression in WT and POLG BMDMs after 4 hours of ISD transfection (2 μg/ml). Statistical significance was determined using unpaired Student's *t* tests. $^*P < 0.05$, $^{**}P < 0.01$, and $^{***}P < 0.001$. Error bars represent SEM.

driving hyperinflammatory responses to LPS, aged mutator mice lacking IFN-I receptor subunit 1 (*Ifnar*$^{-/-}$) also had lower circulating levels of many cytokines compared to mutator mice alone (Fig. 3B, rightmost columns).

IFN-I signaling is known to drive peripheral myeloid expansion in murine models of lupus and can modulate Ly6C^{hi} inflammatory monocyte recruitment in both infectious and sterile diseases (*39*–*43*). To next assess whether cGAS-STING–IFN-I activation governs increased peripheral myeloid expansion in mutator mice, we examined CD11b$^+$Ly6C^{hi} monocyte and CD11b$^+$Ly6G$^+$ neutrophil populations in double mutant cohorts. Notably, CD11b$^+$Ly6C^{hi} inflammatory monocyte numbers were progressively lower in

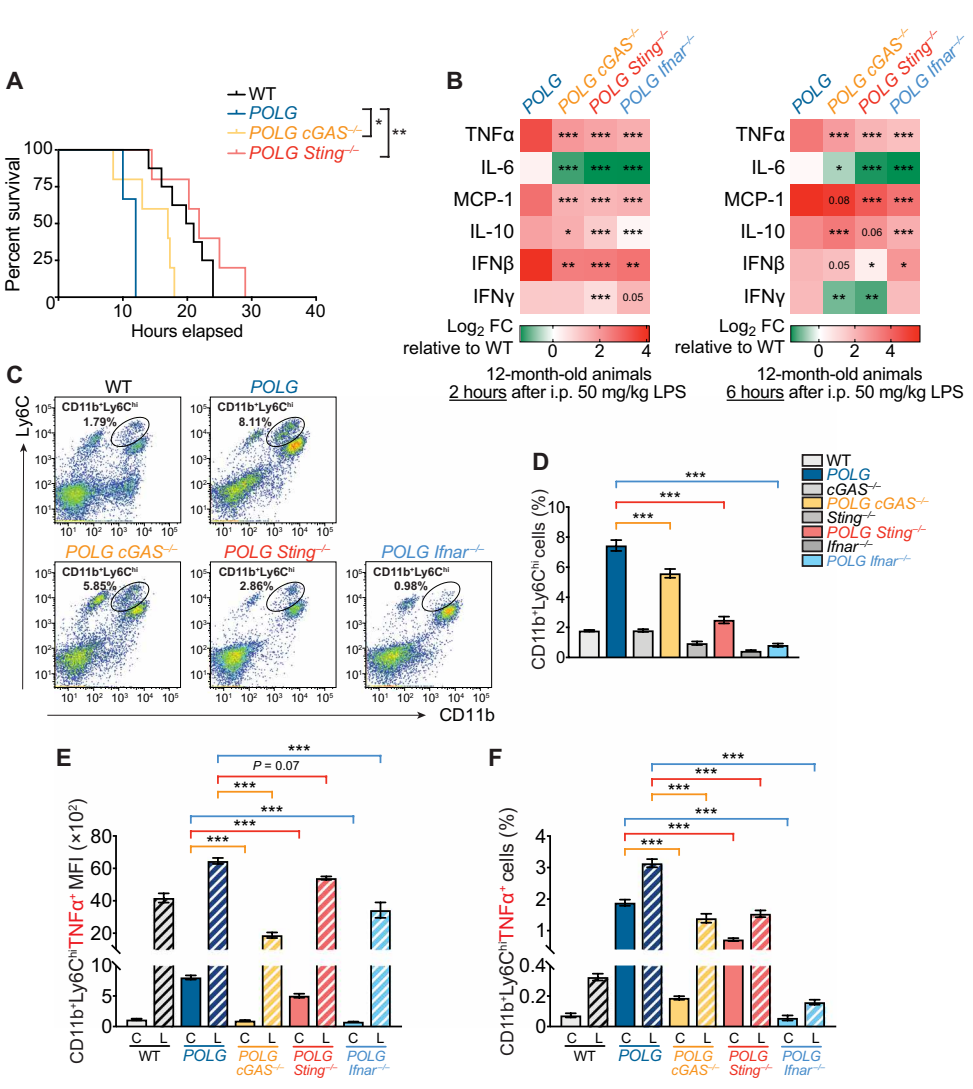

Fig. 3. The cGAS-STING–IFN-I signaling axis regulates inflammatory monocyte expansion and elevated cytokine secretion in POLG mutator mice. (**A** and **B**) Twelve-month-old WT, POLG, POLG *cGAS*$^{-/-}$, POLG *Sting*$^{-/-}$, and POLG *Ifnar*$^{-/-}$ ($n = 5$ to 8 per group) mice were intraperitoneally injected with LPS (50 mg/kg). Kaplan-Meyer survival analysis was performed (A). Plasma was collected at indicated time points ($n \geq 6$ at 2 hours and $n = 4$ at 6 hours) and subjected to multianalyte cytokine analysis (B). Statistical comparisons in (B) were made against LPS-injected POLG mice. Log-rank (Mantel-Cox) test was used to compare percent survival between different groups. (**C** and **D**) CD11b^{+}Ly6C^{hi} inflammatory monocyte population in whole blood from 12-month-old mice was evaluated by flow cytometry. Pseudo-color plots are representative of four independent experiments (C), and quantification of the percentage of CD11b^{+}Ly6C^{hi} cells is shown in (D). (**E** and **F**) CD11b^{+}Ly6C^{hi}TNFα^{+} inflammatory monocyte population in unstimulated or LPS challenged whole blood from 12-month-old cohorts was evaluated by flow cytometry. Quantification of CD11b^{+}Ly6C^{hi}TNFα^{+} MFI is shown in (E), and the percentage of CD11b^{+}Ly6C^{hi}TNFα^{+} cells is shown in (F). Unless stated, statistical significance was determined using analysis of variance (ANOVA) and Tukey post hoc test. *$P < 0.05$, **$P < 0.01$, and ***$P < 0.001$. Error bars represent SEM.

cGAS-, STING-, and IFNAR-deficient mutators (Fig. 3, C and D), while blood neutrophil abundance was also decreased (fig. S3, A and B). Moreover, both CD11b^{+}Ly6C^{hi} monocytes (Fig. 3, E and F) and CD11b^{+}Ly6G^{+} neutrophils (fig. S3, C and D) from IFNAR-deficient mutators produced less TNFα after ex vivo LPS challenge. In addition, TNFα^{+}IL-1β^{+} double-positive leukocytes were decreased in IFNAR-deficient mutator blood after LPS challenge (fig. S3E), and the elevated percentage of CD11b^{+}Ly6C^{hi}TNFα^{+} cells in LPS-stimulated mutator bone marrow was ablated by IFNAR knockout (fig. S3F). Collectively, these results suggest that sustained cGAS-STING–IFN-I signaling in POLG mutator mice promotes peripheral myeloid expansion and innate immune rewiring that potentiates systemic inflammatory responses and increases mortality to LPS challenge.

Antioxidant and anti-inflammatory NRF2 signaling is suppressed in POLG mutator macrophages

To next define the mechanisms underlying elevated ISG and proinflammatory cytokine expression in mutator monocytes and macrophages, we assayed key steps in NF-κB, IRF, and STAT1 activation during a 24-hour LPS time course. Although pathway analysis suggested potentiated signaling in mutator macrophages (fig. S2A), the kinetics of NF-κB, IRF, and STAT1 activation were nearly identical between WT and mutator BMDMs following LPS treatment (fig. S4A). However, in agreement with RNA-seq data implicating elevated glycolytic metabolism, we observed a marked increase in the extracellular acidification rate (ECAR) and decreased basal and maximal oxygen consumption rates (OCRs) in mutator BMDMs

(fig. S4, B and C). This suggested metabolic reprogramming away from mitochondrial respiration to glycolysis for enhanced inflammatory M1 macrophage activation. A recent study reported that the NRF2 transcription factor interferes with LPS-induced cytokine gene expression and is therefore a major transcriptional repressor of M1 macrophage polarization and inflammation (*44*). Our RNA profiling indicated that numerous NRF2-target genes were transcriptionally repressed in mutator macrophages (Fig. 4A and fig. S2A). In agreement, analysis of endogenous NRF2 by quantitative fluorescent microscopy revealed markedly lower nuclear translocation in LPS-stimulated POLG mutator macrophages (Fig. 4, B to D).

To next explore whether NRF2 suppression contributes to hyperinflammatory phenotypes in mutator macrophages, we used three pharmacological approaches to enhance NRF2 activity (*45*–*48*). Treatment of PerMacs with KI696, 4-octyl-itaconate, and dimethyl fumarate (DMF) restored NRF2 target gene expression (Fig. 4E and fig. S4D), suppressed TNFα and IL-6 hyperproduction (Fig. 4, F and G, and fig. S4E), and reduced ISGs in mutator macrophages (fig. S4F). We noted that Kelch-like ECH-associated protein 1 (KEAP1) protein was elevated in mutator macrophages after LPS stimulation (Fig. 4H and fig. S4F). Therefore, we directly targeted KEAP1 in BMDMs by small interfering RNA (siRNA) knockdown and observed a decrease in TNFα after LPS challenge, which was more pronounced in mutator macrophages (Fig. 4I). DMF also limits aerobic glycolysis and lowers cytokine secretion from activated macrophages by inactivating glyceraldehyde-3-phosphate dehydrogenase (GAPDH) (*47*). Accordingly, DMF reduced the elevated GAPDH protein expression in PerMacs from mutator mice (fig. S4F), while also reducing aerobic glycolysis in both WT and mutator macrophages (fig. S4G). Together, these data indicate that NRF2 suppression and augmented aerobic glycolysis shift POLG mutator macrophages toward a more proinflammatory state.

IFN-I signaling represses NRF2 activity and drives proinflammatory metabolic phenotypes in POLG mutator macrophages

NRF2 has been recently reported to inhibit STING-dependent IFN-I responses (*49*–*51*), and IFN-I signaling can limit microbial clearance by dysregulating NRF2 target gene expression (*52*, *53*). To more closely examine how elevated IFN-I signaling may alter the KEAP1-NRF2 axis, we performed a series of experiments in WT BMDMs. Following pretreatment of WT BMDMs with recombinant mouse interferon beta (mIFNβ), we observed that *Keap1* transcripts and protein were elevated in an IFNAR-dependent fashion (fig. S5, A and B). KEAP1 RNA and protein levels were markedly decreased in *Ifnar*$^{-/-}$ macrophages at rest (fig. S5, A and B). *Nrf2* expression was not affected by IFN-I signaling; however, NRF2 protein levels were suppressed by mIFNβ treatment in a dose- and IFNAR-dependent fashion (fig. S5, A and B), suggesting posttranslational turnover due to elevated KEAP1. It is known that TLR4 signaling suppresses KEAP1 expression to stabilize and activate NRF2 (*54*), a finding that we confirmed in WT BMDMs (fig. S5D). However, we noted that pretreatment of BMDMs with mIFNβ resulted in a failure to appropriately down-regulate KEAP1 after LPS, leading to lower overall NRF2 levels, nuclear abundance, and transcriptional activity (fig. S5, C to E). Notably, all of the aforementioned effects were dependent of IFNAR signaling. Together, these results strongly support a model whereby IFN-I signaling directly regulates KEAP1 levels, leading to NRF2 degradation (fig. S5F).

We next used IFNAR-deficient cohorts to examine whether hyperactive IFN-I signaling drives NRF2 suppression in mutator macrophages. We first confirmed that IFNAR depletion ablated elevations in LPS-induced ISG expression in mutator macrophages (Fig. 5A). Then, we used quantitative fluorescent microscopy and observed that *Ifnar*$^{-/-}$ mutator macrophages displayed marked restoration of NRF2 nuclear translocation after LPS challenge (Fig. 5, B to D, and fig. S6, A to C). RNA and protein profiling of NRF2 targets further confirmed that ablation of IFNAR was sufficient to restore, or even hyperactivate, NRF2 signaling in *Ifnar*$^{-/-}$ mutator macrophages (Fig. 5, E and F, and fig. S6D). In addition, the secretion of TNFα and IL-6 cytokines from *Ifnar*$^{-/-}$ mutator macrophages was lowered (Fig. 5G and fig. S6E), further confirming our intracellular cytokine staining results (Fig. 3 and fig. S3).

Consistent with prior findings documenting an anti-inflammatory role of NRF2 (*44*), we observed that siRNA knockdown of NRF2 increased LPS-stimulated TNFα and IL-6 secretion from WT BMDMs relative to control siRNA-transfected cells (Fig. 5, H and I). However, because of basally repressed NRF2 activity in mutator BMDMs, further knockdown of NRF2 did not augment proinflammatory cytokine secretion over control siRNA-transfected POLG BMDMs (Fig. 5I). In contrast, NRF2 knockdown in *Ifnar*$^{-/-}$ mutator BMDMs potentiated proinflammatory cytokine production up to 150% compared to control siRNA-transfected cells (Fig. 5I), suggesting that IFN-I–mediated suppression of NRF2 activity contributes to the hyperinflammatory profile of mutator macrophages and mice. In line with a role for NRF2 antioxidant programs in regulating both mitochondrial and cytosolic ROS (*55*), we detected higher levels of mitochondrial superoxide and total cellular ROS in mutator BMDMs after LPS induction. IFNAR depletion lowered ROS in WT macrophages and markedly reduced ROS in POLG mutator BMDMs (Fig. 5J and fig. S6, F and G). Overall, these results highlight that IFN-I–mediated repression of NRF2, via increased KEAP1 expression, lowers antioxidant capacity and elevates proinflammatory ROS in mutator macrophages.

IFN-I signaling can shift innate immune cell metabolism from OXPHOS to aerobic glycolysis due to induced breaks in the tricarboxylic acid (TCA) cycle (*56*, *57*). Accordingly, we found that IFNβ treatment slightly elevated ECAR in WT BMDMs but markedly increased ECAR in mutator macrophages (fig. S6H). In contrast, knockout of IFNAR markedly reduced ECAR in LPS-stimulated in mutator macrophages, while having little to no effect on WT macrophages (Fig. 5K). Consistent with the changes in ECAR, mutator macrophages had higher lactate dehydrogenase (LDH) expression level and activity and thus produced more L-lactate than WT cells. Ablation of IFN-I signaling in POLG BMDMs largely reversed elevated LDH expression (Fig. 5F) and activity (Fig. 5L) after LPS challenge, while also blunting L-lactate levels (Fig. 5M). Together, our results suggest that blocking IFN-I signaling restores NRF2, lowers oxidative stress and aerobic glycolysis, and blunts the hyperinflammatory profile in POLG mutator macrophages.

Blocking IFN-I signaling restores NRF2 activity, limits oxidative stress, and lowers aerobic glycolysis in aged POLG mutator mice

Several studies have linked oxidative stress to tissue dysfunction and premature aging phenotypes in POLG mutator mice (*29*, *58*–*61*). Therefore, we next explored dysregulation in IFN-I-NRF2 cross-talk in the heart, liver, and kidney of 12-month-old animals. Transcript

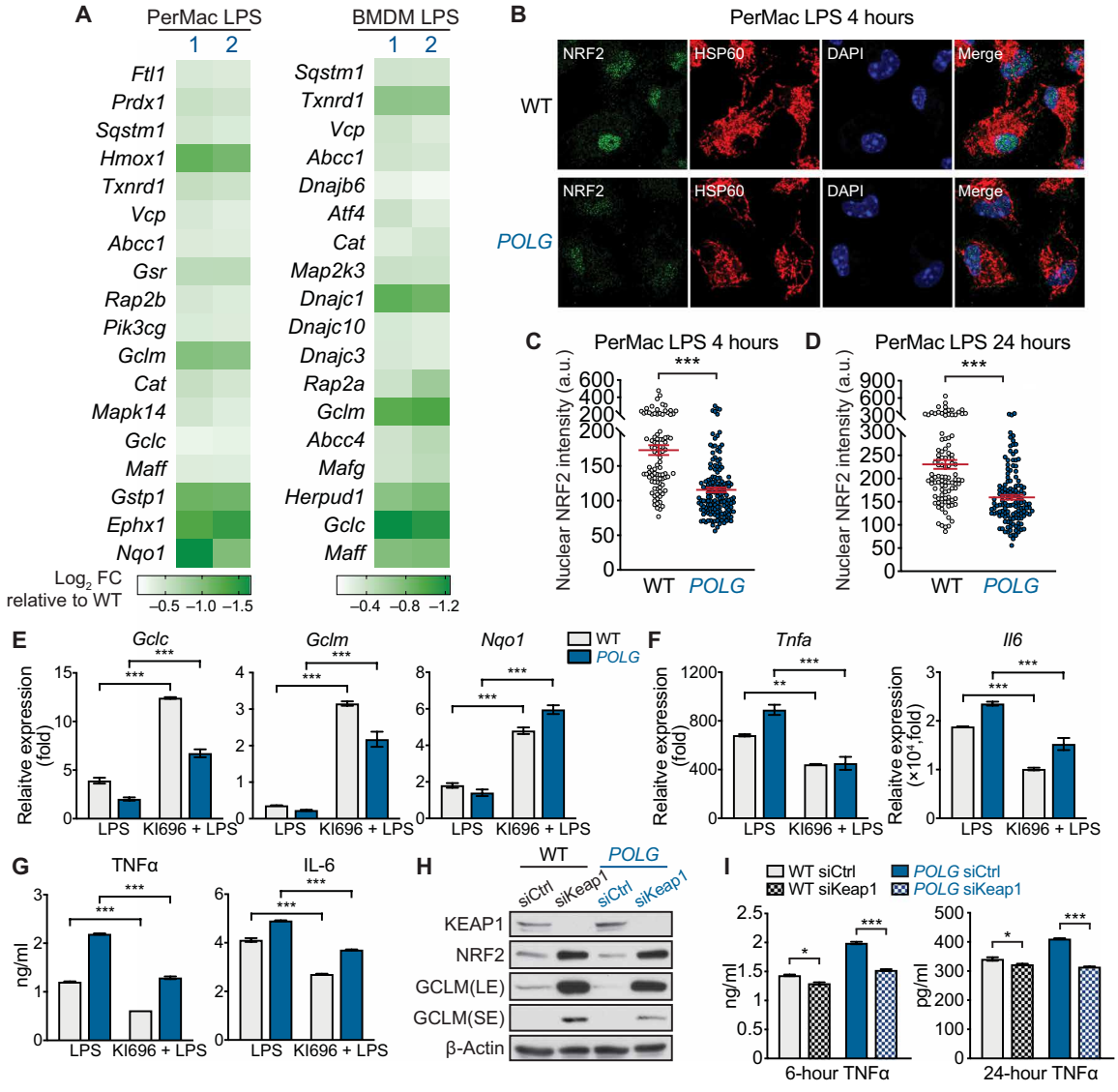

Fig. 4. NRF2 suppression contributes to the hyperinflammatory phenotype of POLG mutator macrophages. (**A**) Heatmaps of RNA-seq data displaying the most down-regulated NRF2 target genes in POLG mutator PerMacs and BMDMs after LPS challenge (200 ng/ml for 6 hours). Log_2 fold changes are relative to WT controls. (**B**) Representative confocal microscopy images of LPS-treated PerMacs stained with anti-NRF2 and anti-HSP60 antibodies and 4′,6-diamidino-2-phenylindole (DAPI). (**C** and **D**) Quantification of nuclear NRF2 staining intensity in WT and POLG PerMacs 4 hours (C) or 24 hours (D) after LPS stimulation. a.u., arbitrary units. (**E** and **F**) qRT-PCR analysis of NRF2 target (E) or proinflammatory cytokine (F) gene expression in WT and POLG PerMacs after LPS or LPS + KI696 treatment. (**G**) Proinflammatory cytokine secretion by WT and POLG PerMacs after LPS or LPS + KI696 treatment. (**H**) Protein expression in siCtrl or siKeap1-transfected WT and POLG BMDMs after LPS treatment (20 ng/ml for 6 hours). SE, short exposure; LE, long exposure. (**I**) TNFα secretion in siCtrl or siKeap1-transfected WT and POLG BMDMs after LPS treatment (20 ng/ml). Statistical significance was determined using unpaired Student's *t* tests (C and D) or ANOVA and Tukey post hoc test (E to G and I). $*P < 0.05$, $**P < 0.01$, and $***P < 0.001$. Error bars represent SEM.

and protein profiling revealed a marked increase in ISGs, similar to that observed in POLG macrophages, which was dependent on intact IFNAR signaling (fig. S7, A and B). In addition, the expression of NRF2 and NRF2-regulated antioxidant genes (*Nqo1*, *Gclc*, *Gclm*, and *Sqstm1/p62*) was markedly lower in mutator tissues compared to age-matched WT littermates but was rescued in *Ifnar*$^{-/-}$ mutator tissues (fig. S7, C and D). Aconitase is widely recognized as a sensitive and specific target of ROS, and aconitase inactivation is a surrogate marker of oxidative stress. Therefore, to determine whether IFN-I–mediated NRF2 suppression increases oxidative stress in mutator mice, we analyzed the enzymatic activity of aconitase in various tissues of WT, mutator, *Ifnar*$^{-/-}$, and *Ifnar*$^{-/-}$ mutator littermate cohorts. Heart, liver, and kidney extracts from mutator mice showed lower aconitase activity, indicative of oxidative stress; however, IFNAR deficiency largely restored aconitase activity in mutator tissues, likely via boosting NRF2-regulated antioxidant activity (fig. S7E).

Our prior observations in macrophages and other reports indicated imbalances in glycolytic metabolism and OXPHOS in mutator tissues (*62*); thus, we next examined expression of enzymes in glycolysis, the TCA cycle, and OXPHOS (fig. S7F). GAPDH and LDHA were elevated in aged POLG mutator tissues (fig. S7F, top);

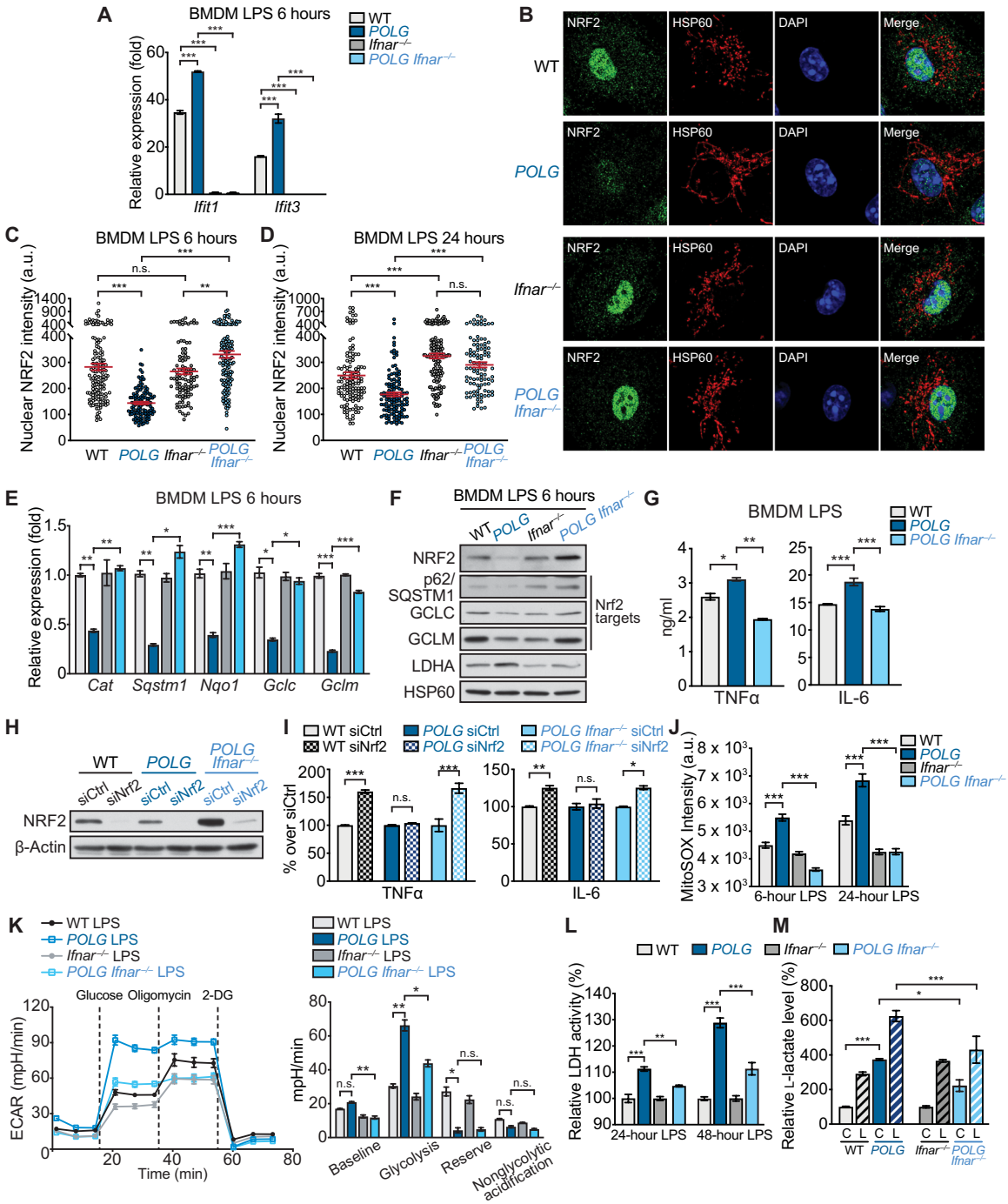

Fig. 5. Elevated IFN-I signaling represses NRF2 activity and drives proinflammatory metabolic phenotypes in POLG mutator macrophages. (**A**) qRT-PCR analysis of ISG expression in BMDMs after LPS challenge. (**B**) Representative confocal microscopy images of LPS-treated BMDMs stained with anti-NRF2 and anti-HSP60 antibodies and DAPI. (**C** and **D**) Quantification of nuclear NRF2 staining intensity in BMDMs 6 hours (C) or 24 hours (D) after LPS exposure. (**E**) qRT-PCR analysis of NRF2 target gene expression in BMDMs after LPS exposure. POLG BMDMs were normalized to WT BMDMs, and POLG *Ifnar*$^{-/-}$ BMDMs were normalized to *Ifnar*$^{-/-}$ BMDMs. (**F**) Protein expression of NRF2 targets and lactate dehydrogenase A (LDHA) in BMDMs after 6-hour LPS (200 ng/ml) exposure. (**G**) Proinflammatory cytokine secretion from WT, POLG, and POLG *Ifnar*$^{-/-}$ BMDMs after LPS stimulation (20 ng/ml for 4 hours). (**H**) Protein expression in siCtrl or siNrf2-transfected WT, POLG, and POLG *Ifnar*$^{-/-}$ BMDMs after LPS treatment (20 ng/ml for 6 hours). (**I**) Proinflammatory cytokines secretion in siCtrl or siNrf2-transfected WT, POLG, and POLG *Ifnar*$^{-/-}$ BMDMs after LPS treatment (20 ng/ml for 24 hours). (**J**) Quantification of MFI of MitoSOX staining in LPS-treated BMDMs. (**K**) Seahorse ECAR analysis of WT, POLG, *Ifnar*$^{-/-}$, and POLG *Ifnar*$^{-/-}$ BMDMs exposed to overnight LPS challenge (10 ng/ml). 2-DG, 2-deoxyglucose. (**L**) Relative LDH activity in BMDMs 24 and 48 hours after LPS exposure (normalized to WT). (**M**) Extracellular L-lactate level in culture media of resting (C) or LPS exposed (L) BMDMs. WT and POLG were normalized to WT resting BMDMs, and *Ifnar*$^{-/-}$ and POLG *Ifnar*$^{-/-}$ were normalized to *Ifnar*$^{-/-}$ resting BMDMs. Statistical significance was determined using ANOVA and Tukey post hoc test. *$P < 0.05$, **$P < 0.01$, and ***$P < 0.001$. n.s., not significant. Error bars represent SEM.

however, *Ifnar*$^{-/-}$ mutator cohorts exhibited decreased glycolytic enzyme expression and decreased L-lactate accumulation in the plasma (fig. S7, F and G). In addition, several TCA cycle enzymes were upregulated in mutator heart and liver homogenates, which may reflect a compensatory response to elevated aerobic glycolysis and OXPHOS deficiency. Consistent with a role for IFN-I–mediated metabolic rewiring, TCA enzymes were largely restored to WT levels in *Ifnar*$^{-/-}$ mutator tissues (fig. S7F, middle). Last, *Ifnar*$^{-/-}$ mutator cohorts exhibited modestly higher levels of some OXPHOS subunits, namely, mitochondrially encoded cytochrome c oxidase I (MT-CO1) and NADH dehydrogenase 1 beta subcomplex subunit 8 (NDUFB8) in the liver, compared to IFNAR-sufficient mutators (fig. S7F, bottom). These findings are consistent with an earlier report showing that elevated IFN-I signaling represses the transcription of mtDNA-encoded genes, leading to reduced OXPHOS complex expression and activity (*63*). Collectively, our tissue analyses mirror the key findings from macrophage studies and thus define chronic IFN-I responses as critical regulators of NRF2 suppression and metabolic/mitochondrial rewiring in POLG mutator mice.

Ablation of IFN-I signaling improves health span and extends life span of POLG mutator mice

Age-related multitissue pathology, including alopecia, kyphosis, anemia, and dilated cardiomyopathy, has been noted in numerous reports on POLG mutator mice (*23*, *24*, *30*, *59*, *64*). As both elevated IFN-I signaling and NRF2 inhibition are implicated in cardiomyopathy and anemia in animal models and human patients (*65*–*68*), we reasoned that sustained imbalances in IFN-I and NRF2 signaling may contribute to the aging-related phenotypes of mutator mice. Using transthoracic echocardiography, we confirmed that 9- to 10-month-old mutator mice exhibited dilated cardiomyopathy by demonstrating left ventricle dilation [wider left ventricular inner diameter at diastole (LVID;d)] and markedly reduced systolic function [decreased left ventricular ejection fraction (LVEF)] (Fig. 6, A and B). Other dilated cardiomyopathy phenotypes included decreased interventricular septum thickness at end-systole (IVS;s), increased left ventricular internal dimension at end-systole (LVID;s), and elevated left ventricular volume at end-systole (Vol;s) (fig. S8, A and B). Cardiac dilation and LVEF were improved in IFNAR-deficient mutator cohorts (Fig. 6, A and B, and fig. S8, A and B). In addition, histological analyses revealed increased mean myofiber width and more infiltrating immune cells in mutator hearts, which were both reduced in IFNAR-deficient mutator sections (Fig. 6, C and D). Last, we noted a shift in the cardiac myosin heavy chain isoform from *Myh6* toward *Myh7* in mutator heart homogenates, which is a well-appreciated marker of cardiac hypertrophy, injury, and stress. Consistent with our echocardiographic and histological measurements, IFNAR-deficient mutator hearts exhibited increased *Myh6* and reduced *Myh7* expression, indicative of lower cardiomyopathy (fig. S8C).

POLG mice develop progressive, ultimately fatal megaloblastic anemia due to hematopoietic stem cell (HSC) deficits, impaired erythrocyte maturation, and increased erythrocyte destruction by splenic macrophages (*30*, *69*, *70*). We found that *Ifnar*$^{-/-}$ mutator blood contains increased cellularity (fig. S8D), as well as higher red blood cell (RBC) counts, hemoglobin (HGB) concentration, and hematocrit (HCT) levels compared to IFNAR-sufficient mutators (Fig. 6E). Moreover, ablation of IFNAR signaling largely restored splenic architecture in POLG mutator mice and increased white pulp to red pulp abundance (Fig. 6F). We also observed widespread extramedullary hematopoiesis in the livers of mutator mice, which was largely ablated in age-matched *Ifnar*$^{-/-}$ mutator cohorts (Fig. 6G), indicating that persistent IFNAR signaling in POLG proofreading-deficient mice contributes to the progressive and lethal anemia observed. Last, we noted that loss of cGAS-STING–IFN-I signaling generally improved body condition in 12-month-old mutator mice, as indicated by less kyphosis of the spine and reduced hair loss (fig. S8E). *Ifnar*$^{-/-}$ mutator cohorts exhibited a 12% extension in mean life span over IFNAR-sufficient mutator mice (Fig. 6, H and I). Together, our data suggest that innate immune reprogramming and chronic IFN-I signaling contribute to age-related anemia and cardiomyopathy, negatively affecting both health span and life span of POLG mutator mice (Fig. 7).

DISCUSSION

Recent clinical case reports suggest that patients with MD experience recurrent infections and develop sepsis and/or SIRS at elevated rates relative to the general population (*14*, *15*, *71*). One study reported that sepsis is the most frequent cause of early death in patients with pediatric MD (*13*). The innate immune system is the first line of defense against invading microbes and is an important driver of hyperinflammatory responses in sepsis and SIRS. However, there is a paucity of information about innate immune system function and/or cellular composition in patients with MDs or murine models. Our work begins to address this critical knowledge gap in a mouse model of POLG-related mitochondrial dysfunction. We have uncovered that POLG mutator mice are highly susceptible to lethal endotoxin shock owing to a marked increase in circulating, myeloid-derived innate immune cell populations and elevated levels of proinflammatory cytokines and IFN-I in the plasma after intraperitoneal LPS challenge. Our data suggest that CD11b^{+} myeloid cell expansion, especially the CD11b^{+}Ly6C^{hi} inflammatory monocyte population, is a key driver of augmented cytokine secretion in mutator mice, as intracellular TNFα levels in CD11b^{+}Ly6C^{hi} mutator monocytes are elevated fourfold compared to WTs. Although mutator mice do not directly model any particular human MD, CD11b^{+} myeloid cell expansion in the bone marrow and spleen has also been observed in the *Ndufs4*$^{-/-}$ model of Leigh syndrome (*72*, *73*). Therefore, future studies in other mouse models and patients are warranted to determine the degree to which monocyte and neutrophil expansion/polarization occurs in MDs. Monitoring circulating MCP-1/CCL2, which is basally elevated in mutator mice and is a predictive biomarker for sepsis, may also aid in identifying MD and elderly/frail populations at risk for developing life-threatening systemic inflammation after infection (*74*, *75*).

Mounting evidence suggests that the IFN-I–driven expansion of inflammatory monocytes is deleterious in autoimmune and inflammatory disorders such as lupus and pneumonia (*39*, *40*, *42*, *76*). Elevated IFN-I signaling during chronic pattern recognition receptor (PRR) stimulation drives HSC skewing toward granulocyte/macrophage progenitors (GMPs), leading to emergency myelopoiesis in the bone marrow and peripheral myeloid expansion (*39*, *77*, *78*). Myeloid lineage skewing in the bone marrow of mutator mice has been previously reported, although the mechanisms underlying this phenotype have remained unclear (*79*). The expansion of Ly6C^{hi} inflammatory monocytes and Ly6G^{+} neutrophils, systemic cytokine levels, and time to death after lethal LPS challenge is substantially reduced in mutator mice lacking cGAS, STING, or IFNAR. We

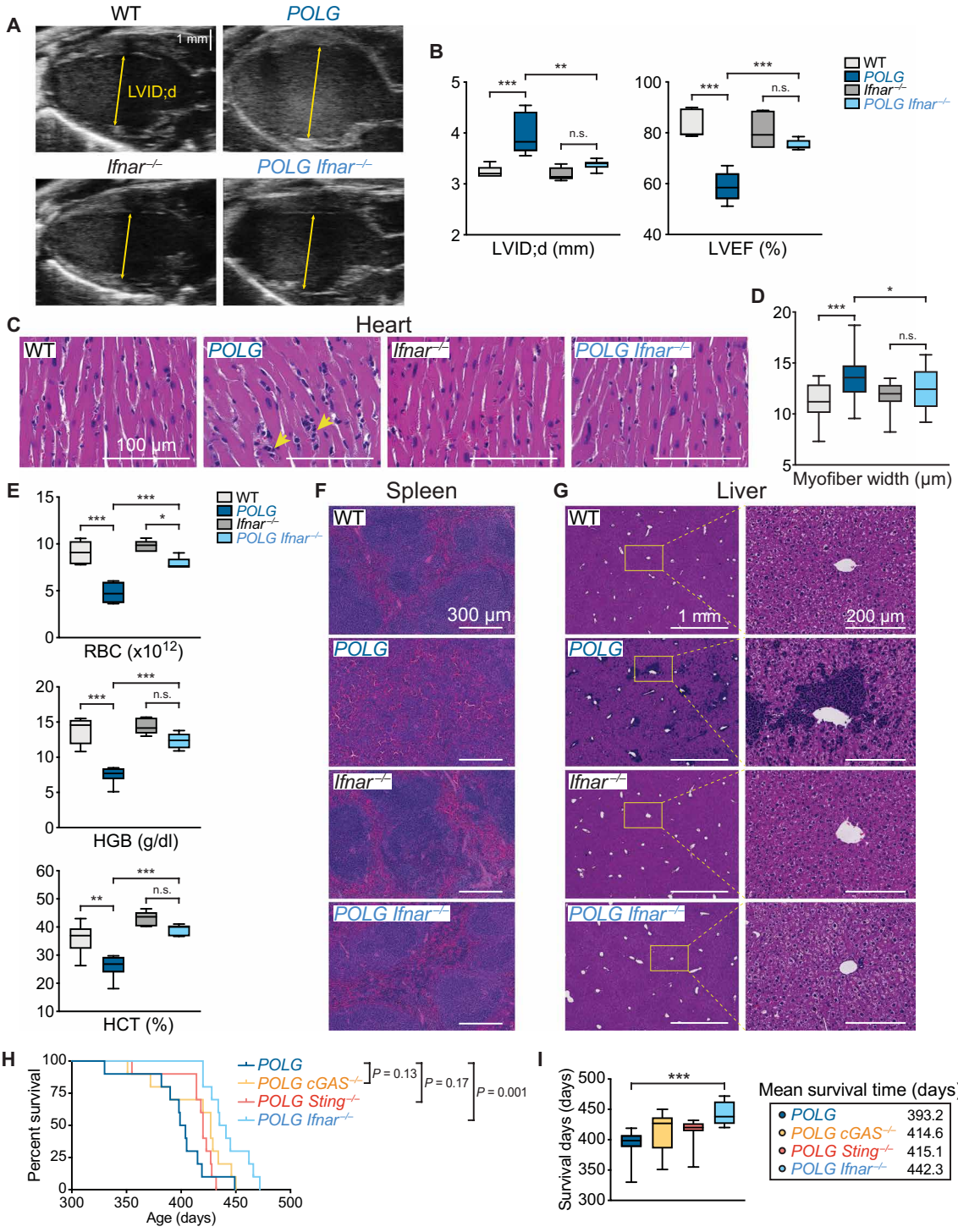

Fig. 6. Ablation of IFN-I signaling lessens multiorgan pathology and extends life span in POLG mutator mice. (**A**) Representative B-mode echocardiogram images of 9- to 10-month-old WT, POLG, *Ifnar*$^{-/-}$, and POLG *Ifnar*$^{-/-}$ mouse hearts. (**B**) LVID;d and LVEF calculated from M-mode or B-mode images using Vevo LAB software. $n = 5$ to 8 animals per genotype. (**C** and **D**) Representative hematoxylin and eosin (H&E) staining of heart sections from WT, POLG, *Ifnar*$^{-/-}$, and POLG *Ifnar*$^{-/-}$ mice (C) and quantification of cardiomyocyte width (D). Yellow arrows indicate infiltrating immune cells. Five myocytes per section and six animals per genotype were quantified in a blinded fashion (D). (**E**) Red blood cell (RBC) counts, hemoglobin (HGB) concentration, and hematocrit (HCT) were measured in WT, POLG, *Ifnar*$^{-/-}$, and POLG *Ifnar*$^{-/-}$ mouse whole blood using the HM5 Hematology Analyzer. $n = 6$ animals per genotype. (**F**) Representative H&E staining showing white pulp and red pulp organization in WT, POLG, *Ifnar*$^{-/-}$, and POLG *Ifnar*$^{-/-}$ mouse spleens. (**G**) Representative H&E-stained liver sections from WT, POLG, *Ifnar*$^{-/-}$, and POLG *Ifnar*$^{-/-}$ cohorts. (**H** and **I**) Percent survival (H) and survival time (I) of POLG, POLG *cGAS*$^{-/-}$, POLG *Sting*$^{-/-}$, and POLG *Ifnar*$^{-/-}$ mice. Log-rank (Mantel-Cox) test was used to compare percent survival between different groups. $n = 10$ animals per genotype. Unless stated, statistical significance was determined using ANOVA and Tukey post hoc test.*$P < 0.05$, **$P < 0.01$, and ***$P < 0.001$. n.s., not significant. Error bars represent SEM.

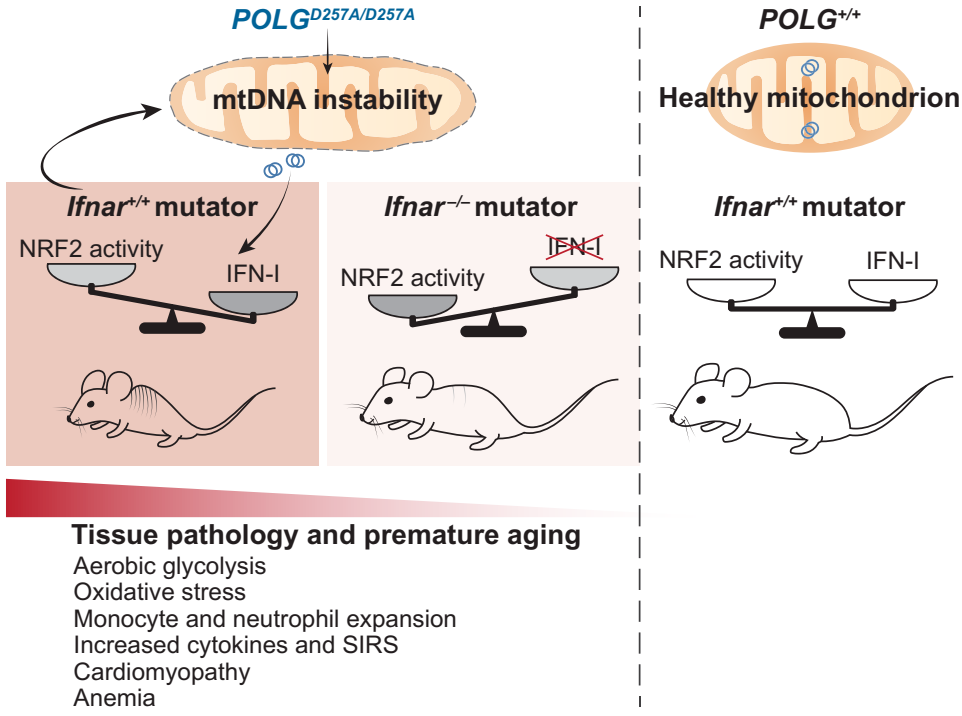

Fig. 7. Imbalances in IFN-I and NRFf2 signaling contribute to inflammatory and age-related phenotypes in POLG mutator mice. mtDNA instability and mitochondrial dysfunction in POLG mutator mice lead to elevated IFN-I responses, which subsequently repress NRF2 activity and enhance aerobic glycolysis. Consequently, chronic IFN-I responses augment the expansion and inflammatory potential of CD11b$^+$ myeloid cells and macrophages, while also contributing to cardiomyopathy and anemia in mutator mice. Genetic ablation of IFN-I signaling relieves the break on NRF2 and markedly improves health span by limiting myeloid reprogramming, inflammation, and tissue dysfunction in mtDNA mutator mice.

therefore propose that mtDNA instability and release in POLG mutators trigger cGAS-STING–dependent IFN-I priming, which not only drives HSC skewing and peripheral myeloid expansion but also potentiates responsiveness of circulating monocytes and neutrophils to innate immune stimuli. However, additional studies are required to clarify the cellular sources of mtDNA and mechanisms of release in mutator mice, while also examining the contribution of nuclear DNA damage to elevated innate immune and IFN-I signaling in this model.

We have found that mutator macrophages are broadly hyperresponsive to PRR agonists, although, unexpectedly, the signaling kinetics of NF-κB, IRF, and STAT1 are nearly identical between WT and mutator BMDMs following LPS treatment. Instead, our data indicate that the hyperinflammatory phenotype of mutator macrophages results from enhanced M1 polarization due to IFN-I–dependent NRF2 suppression and metabolic rewiring. NRF2 can directly inhibit LPS-induced cytokine gene expression, and loss of NRF2 activity is linked to mitochondrial dysfunction and increased glycolysis (*44*, *80*). Compared to cells from age-matched mutator cohorts, IFNAR-deficient mutator macrophages display higher NRF2 levels and target gene expression, while also generating less ROS and proinflammatory cytokines after LPS challenge. This marked restoration in NRF2 activity in *Ifnar*$^{-/-}$ mutators is likely due to a lessening of IFN-I– and IL-10–mediated TCA cycle breaks (i.e., reduced aconitase and isocitrate dehydrogenase activity), which lower carbon flux toward itaconate (*57*). However, consistent with findings in fibroblasts and induced pluripotent stem cells (*60*, *62*), POLG mutator BMDMs also exhibit elevated ECAR and decreased OCR at rest. Thus, the restoration of NRF2 activity in *Ifnar*$^{-/-}$ mutator macrophages may also be due to reduced aerobic glycolysis, which directs pyruvate away from TCA metabolism toward lactate generation. Consistent with this notion, loss of IFN-I signaling markedly blunts ECAR and lactate levels in *Ifnar*$^{-/-}$ mutator macrophages and also lowers plasma lactate concentrations in aged mice. In sum, our results support a model whereby mtDNA mutagenesis in POLG mutator macrophages potentiates IFN-I signaling, which enhances KEAP1 to destabilize NRF2, while also elevating LDHA levels and activity to potentiate aerobic glycolysis.

Our research has also uncovered that elevated IFN-I responses and reduced NRF2 activity extend to multiple organs of aged mutator mice. Genetic ablation of IFNAR is sufficient to blunt potentiated ISG expression and markedly increase NRF2 target gene abundance in the heart, liver, and kidney of aged cohorts. ROS and oxidative stress have been linked to organ dysfunction in aged POLG mice, with antioxidant therapy providing some benefits to overall health span (*29*, *58*, *61*, *69*). We found that markers of oxidative stress are lower in *Ifnar*$^{-/-}$ mutator organs compared to IFNAR-sufficient cohorts, suggesting that IFN-I signaling triggered by mtDNA mutagenesis and instability inhibits NRF2-mediated antioxidant responses in vivo. NRF2-null mice display a spectrum of pathology that overlaps with POLG mutator mice, namely, anemia, splenomegaly, cardiomyopathy, and increased susceptibility to lethal septic shock (*68*, *81*, *82*). Moreover, reduced NRF2 activity is linked to numerous aging-related diseases (*83*–*85*), and NRF2 repression was recently uncovered as a driver of oxidative stress and premature aging in Hutchinson-Gilford progeria syndrome (HGPS) (*86*). Elevated IFN-I

responses have also been observed in HGPS and other progeroid syndromes, which share some overlapping phenotypes with mtDNA mutator mice (*87*–*89*). Notably, we found that *Ifnar*$^{-/-}$ mutator cohorts exhibit an extension in mean survival time of roughly 50 days and an overall improvement under body condition compared to IFNAR-sufficient mutators, documenting that perturbed IFN-I–NRF2 crosstalk is an unappreciated molecular mechanism contributing to premature aging in mutator mice.

Cardiac and hematologic analyses indicate that blockade of IFNAR signaling during aging yields notable improvements in cardiomyopathy and anemia-related phenotypes in mutator mice. Mitochondrial ROS contributes to cardiomyopathy in mutator mice (*59*), and our genetic and echocardiographic data suggest that shifting the balance from IFN-I toward NRF2 activity lowers cardiac oxidative stress and improves cardiac function in aged mutator animals. However, additional IFN-I–dependent inflammatory and metabolic processes are likely dysregulated in aged mutator hearts. Future research on the mutator strains described here should yield new insight into roles for IFN-I dysregulation in both aging- and MD-related cardiomyopathy. Elevated IFN-I signaling has also been linked to anemia in aging and in various human diseases and animal models (*66*, *78*, *90*). A recent report characterized a unique subset of splenic hemophagocytes that differentiate from IFN-I expanded Ly6C^{hi} monocytes, which are responsible for anemia in a model of macrophage activation syndrome and lupus (*39*, *78*). As we observed the IFN-I–dependent elevation of Ly6C^{hi} monocytes in mutator mice, it is likely that the restoration of peripheral erythrocyte numbers in *Ifnar*$^{-/-}$ mutator blood results from less GMP skewing in the bone marrow and reduced destruction of erythrocytes by inflammatory hemophagocytes. Anemia is a frequent hematological abnormality observed in both patients with MD and the elderly, and the presence of anemia negatively influences survival in patients with POLG-related disease (*91*, *92*). Our work provides a strong rationale for translational research to explore whether IFN-I–NRF2 signaling imbalances potentiate anemia in elderly/frail populations and patients with POLG-related MD.

In conclusion, we report that mtDNA mutator mice exhibit a hyperinflammatory innate immune status that is driven by chronic IFN-I priming and NRF2 repression (Fig. 7). Our work constitutes the first detailed characterization of innate immune rewiring in the mutator model and may provide a mechanistic framework for understanding why some patients with MD and the elderly/frail population are more prone to developing sepsis and SIRS following infection. Moreover, we have found that innate immune dysregulation and IFN-I–mediated inflammaging contribute to several progeroid phenotypes in mutator mice. Therapeutic approaches aimed at rebalancing IFN-I–NRF2 signaling may therefore represent a promising target for limiting runaway inflammation, combatting anemia, and improving overall health span in progeroid syndromes, mitochondrial disorders, and aging.

MATERIALS AND METHODS

Mouse strains

C57BL/6J, *POLG*$^{D257A/D257A}$ mutator, *cGAS*$^{-/-}$, *Sting*$^{-/-}$ (*Tmem173*^{gt}), and *Ifnar1*$^{-/-}$ mice were purchased from the Jackson laboratory and bred and maintained in multiple vivaria at Texas A&M University. *POLG*$^{D257A/+}$ breeder pairs used to generate *POLG*$^{+/+}$ and *POLG*$^{D257A/D257A}$ experimental mice (and *cGAS*-, *Sting*-, and *Ifnar*-null intercrosses) were obtained from male *POLG*$^{D257A/+}$ to female C57BL/6J (or *cGAS*-, *Sting*-, and *Ifnar*-null on a pure C57BL/6J background) crosses. All animal experiments were approved by the Institutional Animal Care and Use Committee (IACUC) at Texas A&M University.

Antibodies and reagents

Anti-Interferon-induced protein with tetratricopeptide repeats 3 (IFIT3) was a gift from G. Sen at Cleveland Clinic, and anti-VIPERIN was a gift from P. Cresswell at Yale School of Medicine. Commercially obtained antibodies and reagents include the following antibodies for immunoblotting: rabbit anti-TANK-binding kinase 1 (TBK1) (3504), anti–p-TBK1 (5483), anti-STAT1 (9172), anti–p-STAT1 (7649), anti–Retinoic acid-inducible gene I (RIG-I) (4200), anti–p–inhibitor of NF-κBα (IκBα) (2859), anti-IκBξ (93726), anti-IRF1 (8478), anti-Immune-responsive gene 1 (IRG1) (17805), anti-NRF2 (12721), and anti-KEAP1 (8047) (from Cell Signaling Technology); rabbit anti-LDHA (19987-1-AP), anti-p62/Sequestosome 1 (SQSTM1) (18420-1-AP), anti-IκBα (10268-1-AP), mouse anti-GAPDH (600004-1), and anti–β-actin (66009-1) (from ProteinTech); mouse anti-OXPHOS (ab110413), rabbit anti-Glutamate—cysteine ligase catalytic subunit (GCLC) (ab207777), and anti-Pyruvate dehydrogenase (PDH) (ab110333) (from Abcam); mouse anti-ACO2 (MA1-029) and rabbit anti-Glutamate-cysteine ligase regulatory subunit (GCLM) (MA5-32783) (from Invitrogen); goat anti-60kDa heat shock protein, mitochondrial (HSP60) (N-20) (from Santa Cruz Biotechnology); and rabbit-Alpha-ketoglutarate dehydrogenase (OGDH) (HPA020347) (from Sigma-Aldrich). Antibodies and reagents used for flow cytometry included the following: phycoerythrin/Cy7 anti-mouse TNFα antibody (506324), PerCP/Cy5.5 anti-mouse Ly6C antibody (128012), fluorescein isothiocyanate anti-mouse Ly6C antibody (128006), and PerCP/Cy5.5 anti-mouse IL-12/IL-23 p40 (505211) (from BioLegend); purified anti-mouse CD16 / CD32 (2.4G2) (70-0161), violetFluor 450 anti-mouse Ly6G (1A8) (75-1276), and allophycocyanin anti-human/mouse CD11b (M1/70) (20-0112) (from Tonbo); IL-6 (11-7061-81) (from Invitrogen); IL-1β (31202) (from Cell Signaling Technology); brefeldin A solution (420601) and monensin solution (420701) (from BioLegend); mouse TNFα (430904) and IL-6 (431304) enzyme-linked immunosorbent assay (ELISA) kits (from BioLegend); and Griess Reagent System (G2930) (from Promega).

Cell culture

L929 cells were obtained from American Type Culture Collection and maintained in Dulbecco's modified Eagle's medium (DMEM; D5796, Sigma-Aldrich) supplemented with 10% fetal bovine serum (FBS; 97068-085, VWR). BMDMs were generated from bone marrow and cultured on petri plates in DMEM containing 10% FBS and 30% L929 culture media for 7 days. PerMacs were collected from peritoneal gavages 4 days after intraperitoneal injection of 3% brewer thioglycolate medium (B2551, Sigma-Aldrich). Transfection of ISD (InvivoGen) into the cytosol of BMDMs was performed using polyethyleneimine (43896, Alfa Aesar). Unless stated, 6×10^5 BMDMs and 1.2×10^6 PerMacs per milliliter were used in in vitro experiments. The LPS-B5 Ultrapure (InvivoGen) concentration used was 200 ng/ml for BMDMs and 20 ng/ml for PerMacs unless otherwise indicated. The 4-octyl-itaconate (Cayman) concentration used was 125 μM, the DMF (Sigma-Aldrich) concentration was 50 μM, and the KI696 (MedChemExpress) concentration was 20 μM. Cells were exposed to both treatments 6 hours before LPS stimulation.

siRNA transfection in primary BMDMs

A total of 6×10^5 BMDMs were seeded in 12-well plates the night before transfection. Twenty five nanomolars of siRNA and 3 μl of LipoRNAiMAX (13778150, Thermo Fisher Scientific) were mixed, incubated at room temperature for 10 min, and then added into the wells with plain DMEM. Six hours later, the wells were replenished with complete medium.

LPS in vivo challenge and multianalyte cytokine analysis

Mice were intraperitoneally injected with LPS from *Escherichia coli* O55:B5 (L4005, Sigma-Aldrich). Blood was collected using EDTA-coated tubes at indicated time and then centrifuged at 1000*g* for 15 min at 4°C. The upper phase of plasma was saved and subjected to LEGENDplex Anti-Virus Response Panel (740446, BioLegend) or LEGENDplex Mouse Inflammation Panel (740446, BioLegend) for cytokine analysis.

Blood and bone marrow staining for flow cytometry

The whole mouse blood was collected in sodium heparin tubes, and the bone marrow was harvested from femurs and tibia. RBCs were lysed twice with ACK lysis buffer, and leukocytes were subjected to LPS stimulation (1 μg/ml) in the presence of brefeldin A and monensin for 4 hours. Fc receptors were blocked with anti-mouse CD16/CD32 (2.4G2) antibody, and cells were stained with antibodies against surface proteins, permeabilized with Foxp3/Transcription Factor Staining Buffer Kit (TNB-0607-KIT, Tonbo), and stained with antibodies against intracellular proteins. Cells were analyzed with a BD LSRFortessa X-20.

L. monocytogenes infections

Age- and sex-matched mice of indicated genotypes were used for infections, which were performed under Biosafety level 2 (BSL2) containment according to protocols approved by the Texas A&M IACUC. Two days before infection, cages' plain water bottles were replaced with bottles containing streptomycin (5 mg/ml) in water. The night before infection, chow was removed from the mouse cages. Mice were infected with log-phase (optical density at 600 nm = 0.5 to 1.0) *L. monocytogenes* (strain 10403S, gift from D. Portnoy) grown in Brain heart infusion (BHI) broth at 37°C. Bacteria were washed twice with warm, sterile phosphate-buffered saline (PBS), and for each mouse, an inoculum of 1×10^8 bacteria was placed on a 3-mm piece of bread with 3 ml of butter. Each mouse was individually fed one piece of *Listeria*-soaked bread and butter and then returned to their cage with fresh, antibiotic-free water and chow. Colonization was confirmed by assessing bacterial shedding in feces; at indicated time points, stools were collected from each mouse, dissolved in PBS, and spot-plated as serial dilutions on LB plates. Mice were weighed before infection and regularly throughout to monitor their health status. Bacterial burdens in spleens were determined by homogenizing spleens in 0.1% IGEPAL and plating serial dilutions on LB plates. Plasma was collected using EDTA-coated tubes at indicated time points for cytokine analyses.

Quantitative polymerase chain reaction

To measure relative gene expression by qRT-PCR in cells and tissues, total cellular RNA was isolated using Quick-RNA microprep kit (Zymo Research). Approximately 0.5 to 1 μg of RNA was isolated, and complementary DNA (cDNA) was generated using the qScript cDNA Synthesis Kit (Quanta). cDNA was then subjected to qPCR using PerfeCTa SYBR Green FastMix (Quanta). Three technical replicates were performed for each biological sample, and expression values of each replicate were normalized against Rpl37 cDNA using the $2^{-\Delta\Delta CT}$ method. For mtDNA abundance assessment, template DNA (2 ng/μl) was used for qRT-PCR, and expression values of each replicate were normalized against nuclear-encoded *Actb*. All primer sequences used for qRT-PCR can be found in table S1.

Immunoblotting

Cells and tissues were lysed in 1% NP-40 lysis buffer or 1% SDS lysis buffer supplemented with protease inhibitor and then centrifuged at 4°C to obtain cellular lysate. After bicinchoninic acid assay (BCA) protein assay (Thermo Fisher Scientific), equal amounts of protein (10 to 40 μg) were loaded into 10 to 20% SDS–polyacrylamide gel electrophoresis gradient gels and transferred onto 0.22 μM polyvinylidene difluoride membranes. After air-drying to return to a hydrophobic state, membranes were incubated in primary antibodies at 4°C overnight in 1× PBS containing 1% casein and horseradish perixodase (HRP)–conjugated secondary antibody at room temperature for 1 hour and then developed with Luminata Crescendo Western HRP Substrate (Millipore).

Enzyme-linked immunosorbent assay

Detached cells and debris were removed in cell culture supernatant or plasma before the assay by centrifugation. After incubating in capture antibodies at 4°C overnight, blocking with PBS containing 10% FBS at room temperature for 1 hour, standards and cell culture supernatant were added into the ELISA plates, followed by incubation of detection antibodies, Avidin-HRP, and trimethylboron for faster color development. Plates were washed with PBS containing 0.05% Tween 20 between each step.

Immunofluorescence microscopy

Cells were grown on coverslips and treated as described. After washing in PBS, cells were fixed with 4% paraformaldehyde for 20 min, permeabilized with 0.1% Triton X-100 in PBS for 5 min, blocked with PBS containing 5% FBS for 30 min, stained with primary antibodies for 1 hour, and stained with secondary antibodies for 1 hour. Cells were washed with PBS containing 5% FBS between each step. Coverslips were mounted with ProLong Diamond Antifade Mountant with 4between each step.enylindole (DAPI) (Molecular Probes). Cells were imaged on a LSM 780 confocal microscope (Zeiss) with a 40× or 63× oil-immersed objective with Airyscan or a Cytation 5 (BioTek) with a 20× objective. Three to five images per sample were acquired. At least 100 cells per genotype were used to obtain statistical significance for nuclear Nrf2 intensity analysis. Gen5 software (BioTek) was used to define nuclear region, by DAPI staining, and calculate the Nrf2 fluorescent intensity in the nuclear region of each cell.

Metabolism assays

The Seahorse XFe96 Analyzer was used to measure mitochondrial respiration and glycolysis. Briefly, BMDMs and PerMacs were plated at a density of 5×10^4 cells per well or 2×10^5 cells per well in 80 μl of culture medium in Agilent Seahorse XF96 Cell Culture Microplate. DMF (50 μM) and/or LPS (10 ng/ml) were added 3 hours after the cells were plated. Following a 16-hour incubation, cells were washed and replaced with XF assay medium [Base Medium Minimal DMEM supplemented with 2 mM Ala-Gln (pH 7.4)] before analysis. OCR was measured after sequential addition of 25 mM glucose, 1.5 μM oligomycin, 1.5 μM carbonyl cyanide p-trifluoromethoxyphenylhydrazone +

1 mM sodium pyruvate and 833 nM antimycin A + 833 nM rotenone following a published protocol (*93*). ECAR was measured after sequential addition of 10 mM glucose, 1.5 μM oligomycin and 50 mM 2-DG. OCR measurements 1-15 and ECAR measurements 1-12 of each well were exported and calculated. OCR was determined by: Coupled respiration = average $OCR_{(10,11,12)}$ - average $OCR_{(13,14,15)}$; Uncoupled respiration = average $OCR_{(4,5,6)}$ - average $OCR_{(13,14,15)}$. ECAR was calculated as follows: baseline glycolysis = average $ECAR_{(1,2,3)}$; Glycolysis = average $ECAR_{(4,5,6)}$ - average $ECAR_{(1,2,3)}$; Glycolytic reserve = average $ECAR_{(7,8,9)}$ - average $ECAR_{(4,5,6)}$; non-glycolytic acidification = average $ECAR_{(10,11,12)}$. L-Lactate (700510, Cayman), aconitase (705502, Cayman), and LDH (MK401, TaKaRa) assay kits were commercially purchased. Standard protocols provided with the kits were followed when performing all assays.

Histology

Mice were euthanized and tissues were washed in PBS and incubated for 24 hours in 10% formalin and then transferred to 70% ethanol. Tissue embedding, sectioning, and staining were performed at AML Laboratories in Jacksonville, FL. Images of the hematoxylin and eosin (H&E) staining slides were acquired on Lionheart FX (BioTek) with a 20× or 40× objective. Images for myofiber width quantification were acquired on Nikon ECLIPSE Ts2 and a 40× objective. Ten cells from each sample and three mice of each genotype were imaged and calculated blindly using NIS-Elements software (Nikon).

Echocardiography

Mice were depilated at the chest area the day before echocardiogram measurement. Anesthesia was induced by placing mouse in a box with inhaled isoflurane at 2 to 3%. Afterward, light anesthesia was maintained using a nose cone with inhaled isoflurane at 0.5 to 1%. Mice were immobilized on an instrumented and heated stage. Continuous electric cardiogram, respiration, and temperature (via rectal probe) were monitored. Light anesthesia and core temperature were maintained to ensure near physiological status with heart rate at range of 470 to 520 beats/min. Transthoracic echocardiography was performed using a VisualSonics Vevo 3100 system with a MX550D imaging transducer (center frequency of 40 MHz). Parasternal long-axis (B-mode) and parasternal short-axis (M-mode) views of each animal were taken. Vevo LAB cardiac analysis package was used to analyze the data.

RNA-seq and bioinformatic analyses

Total cellular RNA from WT and POLG BMDMs and PerMacs was prepared using Quick-RNA microprep kit (Zymo Research) and used for the next-generation RNA-seq procedure at Texas A&M University Bioinformatics Core. RNA-seq data were analyzed using BaseSpace Sequence Hub (Illumina). Briefly, Spliced Transcripts Alignment to a Reference (STAR) algorithm of RNA-seq Alignment V2.0.0 software was used to align the results to reference genome *Mus musculus*/mm10 (RefSeq), and then RNA-seq Differential Expression V1.0.0 software was used to obtain raw gene expression files and determine statistically significant changes in gene expression in POLG macrophages relative to WT. Ingenuity Pathway Analysis software (QIAGEN) was used to identify gene families and putative upstream regulators in the datasets. Heatmaps were generated using GraphPad Prism. Raw and analyzed datasets are being deposited into the National Center for Biotechnology Information Gene Expression Omnibus under accession number GSE171960.

Statistical analyses

Error bars displayed throughout the manuscript represent SEM and were calculated from triplicate technical replicates of each biological sample unless otherwise indicated. For ex vivo experiments, error bars were calculated from the average of duplicate or triplicate technical replicates of at least four animals per point. For microscopy quantification, images were taken throughout the slide of each sample using DAPI channel to avoid bias of selection, and at least 100 cells per genotype were randomly selected to obtain statistical significance. To reduce potential experimental bias, samples for cardiac function (LVID;d, LVEF, IVS;s, LVID;s, and Vol;s) and myofiber width analysis in Fig. 6 were blinded to researchers when performing analysis. The identities were only revealed at the final data analysis stage. No randomization or blinding was used for all other animal studies. No statistical method was used to predetermine sample size. Data shown are representative of at least three independent experiments, including microscopy images, Western blots, flow cytometry, and all metabolism assays.

SUPPLEMENTARY MATERIALS

Supplementary material for this article is available at http://advances.sciencemag.org/cgi/content/full/7/22/eabe7548/DC1

View/request a protocol for this paper from *Bio-protocol*.

REFERENCES AND NOTES

1. A. P. West, Mitochondrial dysfunction as a trigger of innate immune responses and inflammation. *Toxicology* **391**, 54–63 (2017).
2. A. P. West, G. S. Shadel, S. Ghosh, Mitochondria in innate immune responses. *Nat. Rev. Immunol.* **11**, 389–402 (2011).
3. S. E. Weinberg, L. A. Sena, N. S. Chandel, Mitochondria in the regulation of innate and adaptive immunity. *Immunity* **42**, 406–417 (2015).
4. E. L. Mills, B. Kelly, L. A. J. O'Neill, Mitochondria are the powerhouses of immunity. *Nat. Immunol.* **18**, 488–498 (2017).
5. R. J. Youle, Mitochondria—Striking a balance between host and endosymbiont. *Science* **365**, eaaw9855 (2019).
6. A. P. West, G. S. Shadel, Mitochondrial DNA in innate immune responses and inflammatory pathology. *Nat. Rev. Immunol.* **17**, 363–375 (2017).
7. A. P. West, W. Khoury-Hanold, M. Staron, M. C. Tal, C. M. Pineda, S. M. Lang, M. Bestwick, B. A. Duguay, N. Raimundo, D. A. MacDuff, S. M. Kaech, J. R. Smiley, R. E. Means, A. Iwasaki, G. S. Shadel, Mitochondrial DNA stress primes the antiviral innate immune response. *Nature* **520**, 553–557 (2015).
8. A. Ablasser, Z. J. Chen, cGAS in action: Expanding roles in immunity and inflammation. *Science* **363**, eaat8657 (2019).
9. K. Nakahira, S. Hisata, A. M. K. Choi, The roles of mitochondrial damage-associated molecular patterns in diseases. *Antioxid. Redox Signal.* **23**, 1329–1350 (2015).
10. Z. Wu, S. Oeck, A. P. West, K. C. Mangalhara, A. G. Sainz, L. E. Newman, X.-O. Zhang, L. Wu, Q. Yan, M. Bosenberg, Y. Liu, P. L. Sulkowski, V. Tripple, S. M. Kaech, P. M. Glazer, G. S. Shadel, Mitochondrial DNA stress signalling protects the nuclear genome. *Nat. Metab.* **1**, 1209–1218 (2019).
11. G. S. Gorman, P. F. Chinnery, S. DiMauro, M. Hirano, Y. Koga, R. McFarland, A. Suomalainen, D. R. Thorburn, M. Zeviani, D. M. Turnbull, Mitochondrial diseases. *Nat. Rev. Dis. Primers.* **2**, 16080 (2016).
12. J. D. Stumpf, R. P. Saneto, W. C. Copeland, Clinical and molecular features of *POLG*-related mitochondrial disease. *Cold Spring Harb. Perspect. Biol.* **5**, a011395 (2013).
13. S. Eom, H. N. Lee, S. Lee, H.-C. Kang, J. S. Lee, H. D. Kim, Y.-M. Lee, Cause of death in children with mitochondrial diseases. *Pediatr. Neurol.* **66**, 82–88 (2017).
14. S. M. Kapnick, S. E. Pacheco, P. J. McGuire, The emerging role of immune dysfunction in mitochondrial diseases as a paradigm for understanding immunometabolism. *Metab. Clin. Exp.* **81**, 97–112 (2018).
15. M. A. Walker, N. Slate, A. Alejos, S. Volpi, R. S. Iyengar, D. Sweetser, K. B. Sims, J. E. Walter, Predisposition to infection and SIRS in mitochondrial disorders: 8 years' experience in an academic center. *J. Allergy Clin. Immunol. Pract. Amsterdam* **2**, 465–468.e1 (2014).
16. T. N. Tarasenko, S. E. Pacheco, M. K. Koenig, J. Gomez-Rodriguez, S. M. Kapnick, F. Diaz, P. M. Zerfas, E. Barca, J. Sudderth, R. J. DeBerardinis, R. Covian, R. S. Balaban, S. DiMauro, P. J. McGuire, Cytochrome c oxidase activity is a metabolic checkpoint that regulates cell fate decisions during T cell activation and differentiation. *Cell Metab.* **25**, 1254–1268.e7 (2017).

17. O. Hasselmann, N. Blau, V. T. Ramaekers, E. V. Quadros, J. M. Sequeira, M. Weissert, Cerebral folate deficiency and CNS inflammatory markers in Alpers disease. *Mol. Genet. Metab.* **99**, 58–61 (2010).
18. H. M. Wilkins, I. W. Weidling, Y. Ji, R. H. Swerdlow, Mitochondria-derived damage-associated molecular patterns in neurodegeneration. *Front. Immunol.* **8**, 508 (2017).
19. M. J. Young, W. C. Copeland, Human mitochondrial DNA replication machinery and disease. *Curr. Opin. Genet. Dev.* **38**, 52–62 (2016).
20. S. Rahman, W. C. Copeland, *POLG*-related disorders and their neurological manifestations. *Nat. Rev. Neurol.* **15**, 40–52 (2019).
21. B. Singh, K. M. Owens, P. Bajpai, M. M. Desouki, V. Srinivasasainagendra, H. K. Tiwari, K. K. Singh, Mitochondrial DNA polymerase *POLG1* disease mutations and germline variants promote tumorigenic properties. *PLOS ONE* **10**, e0139846 (2015).
22. G. Davidzon, P. Greene, M. Mancuso, K. J. Klos, J. E. Ahlskog, M. Hirano, S. DiMauro, Early-onset familial parkinsonism due to *POLG* mutations. *Ann. Neurol.* **59**, 859–862 (2006).
23. G. C. Kujoth, A. Hiona, T. D. Pugh, S. Someya, K. Panzer, S. E. Wohlgemuth, T. Hofer, A. Y. Seo, R. Sullivan, W. A. Jobling, J. D. Morrow, H. Van Remmen, J. M. Sedivy, T. Yamasoba, M. Tanokura, R. Weindruch, C. Leeuwenburgh, T. A. Prolla, Mitochondrial DNA mutations, oxidative stress, and apoptosis in mammalian aging. *Science* **309**, 481–484 (2005).
24. A. Trifunovic, A. Wredenberg, M. Falkenberg, J. N. Spelbrink, A. T. Rovio, C. E. Bruder, M. Bohlooly-Y, S. Gidlöf, A. Oldfors, R. Wibom, J. Törnell, H. T. Jacobs, N.-G. Larsson, Premature ageing in mice expressing defective mitochondrial DNA polymerase. *Nature* **429**, 417–423 (2004).
25. N. Nissanka, S. R. Bacman, M. J. Plastini, C. T. Moraes, The mitochondrial DNA polymerase gamma degrades linear DNA fragments precluding the formation of deletions. *Nat. Commun.* **9**, 2491 (2018).
26. S. L. Williams, J. Huang, Y. J. K. Edwards, R. H. Ulloa, L. M. Dillon, T. A. Prolla, J. M. Vance, C. T. Moraes, S. Züchner, The mtDNA mutation spectrum of the progeroid *Polg* mutator mouse includes abundant control region multimers. *Cell Metab.* **12**, 675–682 (2010).
27. K. Szczepanowska, A. Trifunovic, Different faces of mitochondrial DNA mutators. *Biochim. Biophys. Acta Bioenergetics* **1847**, 1362–1372 (2015).
28. J. Y. Jang, A. Blum, J. Liu, T. Finkel, The role of mitochondria in aging. *J. Clin. Invest.* **128**, 3662–3670 (2018).
29. A. Logan, I. G. Shabalina, T. A. Prime, S. Rogatti, A. V. Kalinovich, R. C. Hartley, R. C. Budd, B. Cannon, M. P. Murphy, In vivo levels of mitochondrial hydrogen peroxide increase with age in mtDNA mutator mice. *Aging Cell* **13**, 765–768 (2014).
30. M. L. Chen, T. D. Logan, M. L. Hochberg, S. G. Shelat, X. Yu, G. E. Wilding, W. Tan, G. C. Kujoth, T. A. Prolla, M. A. Selak, M. Kundu, M. Carroll, J. E. Thompson, Erythroid dysplasia, megaloblastic anemia, and impaired lymphopoiesis arising from mitochondrial dysfunction. *Blood* **114**, 4045–4053 (2009).
31. A. Safdar, J. M. Bourgeois, D. I. Ogborn, J. P. Little, B. P. Hettinga, M. Akhtar, J. E. Thompson, S. Melov, N. J. Mocellin, G. C. Kujoth, T. A. Prolla, M. A. Tarnopolsky, Endurance exercise rescues progeroid aging and induces systemic mitochondrial rejuvenation in mtDNA mutator mice. *Proc. Natl. Acad. Sci. U.S.A.* **108**, 4135–4140 (2011).
32. C. Shi, T. M. Hohl, I. Leiner, M. J. Equinda, X. Fan, E. G. Pamer, Ly6G$^+$ neutrophils are dispensable for defense against systemic *Listeria monocytogenes* infection. *J. Immunol.* **187**, 5293–5298 (2011).
33. H. Maekawa, T. Inoue, H. Ouchi, T.-M. Jao, R. Inoue, H. Nishi, R. Fujii, F. Ishidate, T. Tanaka, Y. Tanaka, N. Hirokawa, M. Nangaku, R. Inagi, Mitochondrial damage causes inflammation via cGAS-STING signaling in acute kidney injury. *Cell Rep.* **29**, 1261–1273.e6 (2019).
34. K. W. Chung, P. Dhillon, S. Huang, X. Sheng, R. Shrestha, C. Qiu, B. A. Kaufman, J. Park, L. Pei, J. Baur, M. Palmer, K. Susztak, Mitochondrial damage and activation of the STING pathway lead to renal inflammation and fibrosis. *Cell Metab.* **30**, 784–799.e5 (2019).
35. D. A. Sliter, J. Martinez, L. Hao, X. Chen, N. Sun, T. D. Fischer, J. L. Burman, Y. Li, Z. Zhang, D. P. Narendra, H. Cai, M. Borsche, C. Klein, R. J. Youle, Parkin and PINK1 mitigate STING-induced inflammation. *Nature* **561**, 258–262 (2018).
36. G. Rackov, R. Shokri, M. Á. De Mon, C. Martínez-A., D. Balomenos, The role of IFN-β during the course of sepsis progression and its therapeutic potential. *Front. Immunol.* **8**, 493 (2017).
37. S. H. Park, K. Kang, E. Giannopoulou, Y. Qiao, K. Kang, G. Kim, K.-H. Park-Min, L. B. Ivashkiv, Type I interferons and the cytokine TNF cooperatively reprogram the macrophage epigenome to promote inflammatory activation. *Nat. Immunol.* **18**, 1104–1116 (2017).
38. M. Karaghiosoff, R. Steinborn, P. Kovarik, G. Kriegshäuser, M. Baccarini, B. Donabauer, U. Reichart, T. Kolbe, C. Bogdan, T. Leanderson, D. Levy, T. Decker, M. Müller, Central role for type I interferons and Tyk2 in lipopolysaccharide-induced endotoxin shock. *Nat. Immunol.* **4**, 471–477 (2003).
39. M. B. Buechler, T. H. Teal, K. B. Elkon, J. A. Hamerman, Cutting edge: Type I IFN drives emergency myelopoiesis and peripheral myeloid expansion during chronic TLR7 signaling. *J. Immunol.* **190**, 886–891 (2013).
40. P. Y. Lee, Y. Li, Y. Kumagai, Y. Xu, J. S. Weinstein, E. S. Kellner, D. C. Nacionales, E. J. Butfiloski, N. van Rooijen, S. Akira, E. S. Sobel, M. Satoh, W. H. Reeves, Type I interferon modulates monocyte recruitment and maturation in chronic inflammation. *Am. J. Pathol.* **175**, 2023–2033 (2009).
41. S.-U. Seo, H.-J. Kwon, H.-J. Ko, Y.-H. Byun, B. L. Seong, S. Uematsu, S. Akira, M.-N. Kweon, Type I interferon signaling regulates Ly6C^{hi} monocytes and neutrophils during acute viral pneumonia in mice. *PLOS Pathog.* **7**, e1001304 (2011).
42. R. Channappanavar, A. R. Fehr, R. Vijay, M. Mack, J. Zhao, D. K. Meyerholz, S. Perlman, Dysregulated type I interferon and inflammatory monocyte-macrophage responses cause lethal pneumonia in SARS-CoV-infected mice. *Cell Host Microbe* **19**, 181–193 (2016).
43. O. Majer, C. Bourgeois, F. Zwolanek, C. Lassnig, D. Kerjaschki, M. Mack, M. Müller, K. Kuchler, Type I interferons promote fatal immunopathology by regulating inflammatory monocytes and neutrophils during *Candida* infections. *PLOS Pathog.* **8**, e1002811 (2012).
44. E. H. Kobayashi, T. Suzuki, R. Funayama, T. Nagashima, M. Hayashi, H. Sekine, N. Tanaka, T. Moriguchi, H. Motohashi, K. Nakayama, M. Yamamoto, Nrf2 suppresses macrophage inflammatory response by blocking proinflammatory cytokine transcription. *Nat. Commun.* **7**, 11624 (2016).
45. M. Bambouskova, L. Gorvel, V. Lampropoulou, A. Sergushichev, E. Loginicheva, K. Johnson, D. Korenfeld, M. E. Mathyer, H. Kim, L.-H. Huang, D. Duncan, H. Bregman, A. Keskin, A. Santeford, R. S. Apte, R. Sehgal, B. Johnson, G. K. Amarasinghe, M. P. Soares, T. Satoh, S. Akira, T. Hai, C. de Guzman Strong, K. Auclair, T. P. Roddy, S. A. Biller, M. Jovanovic, E. Klechevsky, K. M. Stewart, G. J. Randolph, M. N. Artyomov, Electrophilic properties of itaconate and derivatives regulate the IκBζ–ATF3 inflammatory axis. *Nature* **556**, 501–504 (2018).
46. E. L. Mills, D. G. Ryan, H. A. Prag, D. Dikovskaya, D. Menon, Z. Zaslona, M. P. Jedrychowski, A. S. H. Costa, M. Higgins, E. Hams, J. Szpyt, M. C. Runtsch, M. S. King, J. F. McGouran, R. Fischer, B. M. Kessler, A. F. McGettrick, M. M. Hughes, R. G. Carroll, L. M. Booty, E. V. Knatko, P. J. Meakin, M. L. J. Ashford, L. K. Modis, G. Brunori, D. C. Sévin, P. G. Fallon, S. T. Caldwell, E. R. S. Kunji, E. T. Chouchani, C. Frezza, A. T. Dinkova-Kostova, R. C. Hartley, M. P. Murphy, L. A. O'Neill, Itaconate is an anti-inflammatory metabolite that activates Nrf2 via alkylation of KEAP1. *Nature* **556**, 113–117 (2018).
47. M. D. Kornberg, P. Bhargava, P. M. Kim, V. Putluri, A. M. Snowman, N. Putluri, P. A. Calabresi, S. H. Snyder, Dimethyl fumarate targets GAPDH and aerobic glycolysis to modulate immunity. *Science* **360**, 449–453 (2018).
48. T. G. Davies, W. E. Wixted, J. E. Coyle, C. Griffiths-Jones, K. Hearn, R. McMenamin, D. Norton, S. J. Rich, C. Richardson, G. Saxty, H. M. G. Willems, A. J.-A. Woolford, J. E. Cottom, J.-P. Kou, J. G. Yonchuk, H. G. Feldser, Y. Sanchez, J. P. Foley, B. J. Bolognese, G. Logan, P. L. Podolin, H. Yan, J. F. Callahan, T. D. Heightman, J. K. Kerns, Monoacidic inhibitors of the Kelch-like ECH-associated protein 1: Nuclear factor erythroid 2-related factor 2 (KEAP1:NRF2) protein–protein interaction with high cell potency identified by fragment-based discovery. *J. Med. Chem.* **59**, 3991–4006 (2016).
49. D. Olagnier, R. R. Lababidi, S. B. Hadj, A. Sze, Y. Liu, S. D. Naidu, M. Ferrari, Y. Jiang, C. Chiang, V. Beljanski, M.-L. Goulet, E. V. Knatko, A. T. Dinkova-Kostova, J. Hiscott, R. Lin, Activation of Nrf2 signaling augments vesicular stomatitis virus oncolysis via autophagy-driven suppression of antiviral immunity. *Mol. Ther.* **25**, 1900–1916 (2017).
50. C. Gunderstofte, M. B. Iversen, S. Peri, A. Thielke, S. Balachandran, C. K. Holm, D. Olagnier, Nrf2 negatively regulates type I interferon responses and increases susceptibility to herpes genital infection in mice. *Front. Immunol.* **10**, 2101 (2019).
51. D. Olagnier, A. M. Brandtoft, C. Gunderstofte, N. L. Villadsen, C. Krapp, A. L. Thielke, A. Laustsen, S. Peri, A. L. Hansen, L. Bonefeld, J. Thyrsted, V. Bruun, M. B. Iversen, L. Lin, V. M. Artegoitia, C. Su, L. Yang, R. Lin, S. Balachandran, Y. Luo, M. Nyegaard, B. Marrero, R. Goldbach-Mansky, M. Motwani, D. G. Ryan, K. A. Fitzgerald, L. A. O'Neill, A. K. Hollensen, C. K. Damgaard, F. v. de Paoli, H. C. Bertram, M. R. Jakobsen, T. B. Poulsen, C. K. Holm, Nrf2 negatively regulates STING indicating a link between antiviral sensing and metabolic reprogramming. *Nat. Commun.* **9**, 3506 (2018).
52. N. J. Hos, R. Ganesan, S. Gutiérrez, D. Hos, J. Klimek, Z. Abdullah, M. Krönke, N. Robinson, Type I interferon enhances necroptosis of *Salmonella* Typhimurium–infected macrophages by impairing antioxidative stress responses. *J. Cell Biol.* **216**, 4107–4121 (2017).
53. M. Riedelberger, P. Penninger, M. Tscherner, M. Seifert, S. Jenull, C. Brunnhofer, B. Scheidl, I. Tsymala, C. Bourgeois, A. Petryshyn, W. Glaser, A. Limbeck, B. Strobl, G. Weiss, K. Kuchler, Type I interferon response dysregulates host iron homeostasis and enhances *Candida glabrata* infection. *Cell Host Microbe* **27**, 454–466.e8 (2020).
54. S. Yin, W. Cao, Toll-like receptor signaling induces Nrf2 pathway activation through p62-triggered Keap1 degradation. *Mol. Cell. Biol.* **35**, 2673–2683 (2015).
55. S. Kovac, P. R. Angelova, K. M. Holmström, Y. Zhang, A. T. Dinkova-Kostova, A. Y. Abramov, Nrf2 regulates ROS production by mitochondria and NADPH oxidase. *Biochim. Biophys. Acta* **1850**, 794–801 (2015).
56. A. Pantel, A. Teixeira, E. Haddad, E. G. Wood, R. M. Steinman, M. P. Longhi, Direct type I IFN but not MDA5/TLR3 activation of dendritic cells is required for maturation and metabolic shift to glycolysis after poly IC stimulation. *PLOS Biol.* **12**, e1001759 (2014).
57. D. P. De Souza, A. Achuthan, M. K. S. Lee, K. J. Binger, M.-C. Lee, S. Davidson, D. L. Tull, M. J. McConville, A. D. Cook, A. J. Murphy, J. A. Hamilton, A. J. Fleetwood, Autocrine IFN-I inhibits isocitrate dehydrogenase in the TCA cycle of LPS-stimulated macrophages. *J. Clin. Invest.* **129**, 4239–4244 (2019).
58. I. G. Shabalina, M. Y. Vyssokikh, N. Gibanova, R. I. Csikasz, D. Edgar, A. Hallden-Waldemarson, Z. Rozhdestvenskaya, L. E. Bakeeva, V. B. Vays, A. V. Pustovidko, M. V. Skulachev,

B. Cannon, V. P. Skulachev, J. Nedergaard, Improved health-span and lifespan in mtDNA mutator mice treated with the mitochondrially targeted antioxidant SkQ1. *Aging (Albany NY)* **9**, 315–336 (2017).
59. D.-F. Dai, T. Chen, J. Wanagat, M. Laflamme, D. J. Marcinek, M. J. Emond, C. P. Ngo, T. A. Prolla, P. S. Rabinovitch, Age-dependent cardiomyopathy in mitochondrial mutator mice is attenuated by overexpression of catalase targeted to mitochondria. *Aging Cell* **9**, 536–544 (2010).
60. R. H. Hämäläinen, K. J. Ahlqvist, P. Ellonen, M. Lepistö, A. Logan, T. Otonkoski, M. P. Murphy, A. Suomalainen, mtDNA mutagenesis disrupts pluripotent stem cell function by altering redox signaling. *Cell Rep.* **11**, 1614–1624 (2015).
61. J. E. Kolesar, A. Safdar, A. Abadi, L. G. MacNeil, J. D. Crane, M. A. Tarnopolsky, B. A. Kaufman, Defects in mitochondrial DNA replication and oxidative damage in muscle of mtDNA mutator mice. *Free Radic. Biol. Med.* **75**, 241–251 (2014).
62. A. Saleem, A. Safdar, Y. Kitaoka, X. Ma, O. S. Marquez, M. Akhtar, A. Nazli, R. Suri, J. Turnbull, M. A. Tarnopolsky, Polymerase gamma mutator mice rely on increased glycolytic flux for energy production. *Mitochondrion* **21**, 19–26 (2015).
63. J. A. Lewis, A. Huq, P. Najarro, Inhibition of mitochondrial function by interferon *. *J. Biol. Chem.* **271**, 13184–13190 (1996).
64. B. P. Woodall, A. M. Orogo, R. H. Najor, M. Q. Cortez, E. R. Moreno, H. Wang, A. S. Divakaruni, A. N. Murphy, Å. B. Gustafsson, Parkin does not prevent accelerated cardiac aging in mitochondrial DNA mutator mice. *JCI Insight* **4**, e127713 (2019).
65. A. Y. Khakoo, M. K. Halushka, J. E. Rame, E. R. Rodriguez, E. K. Kasper, D. P. Judge, Reversible cardiomyopathy caused by administration of interferon α. *Nat. Clin. Pract. Cardiovasc. Med.* **2**, 53–57 (2005).
66. S. Ioannou, G. Hatzis, I. Vlahadami, M. Voulgarelis, Aplastic anemia associated with interferon alpha 2a in a patient with chronic hepatitis C virus infection: A case report. *J. Med. Case Reports* **4**, 268 (2010).
67. J. Chen, Z. Zhang, L. Cai, Diabetic cardiomyopathy and its prevention by nrf2: Current status. *Diabetes Metab. J.* **38**, 337–345 (2014).
68. J.-M. Lee, K. Chan, Y. W. Kan, J. A. Johnson, Targeted disruption of Nrf2 causes regenerative immune-mediated hemolytic anemia. *Proc. Natl. Acad. Sci. U.S.A.* **101**, 9751–9756 (2004).
69. K. J. Ahlqvist, R. H. Hämäläinen, S. Yatsuga, M. Uutela, M. Terzioglu, A. Götz, S. Forsström, P. Salven, A. Angers-Loustau, O. H. Kopra, H. Tyynismaa, N.-G. Larsson, K. Wartiovaara, T. Prolla, A. Trifunovic, A. Suomalainen, Somatic progenitor cell vulnerability to mitochondrial DNA mutagenesis underlies progeroid phenotypes in Polg mutator mice. *Cell Metab.* **15**, 100–109 (2012).
70. K. J. Ahlqvist, S. Leoncini, A. Pecorelli, S. B. Wortmann, S. Ahola, S. Forsström, R. Guerranti, C. De Felice, J. Smeitink, L. Ciccoli, R. H. Hämäläinen, A. Suomalainen, MtDNA mutagenesis impairs elimination of mitochondria during erythroid maturation leading to enhanced erythrocyte destruction. *Nat. Commun.* **6**, 6494 (2015).
71. J. L. Edmonds, D. J. Kirse, D. Kearns, R. Deutsch, L. Spruijt, R. K. Naviaux, The otolaryngological manifestations of mitochondrial disease and the risk of neurodegeneration with infection. *Arch. Otolaryngol. Head Neck Surg.* **128**, 355–362 (2002).
72. A. Quintana, S. E. Kruse, R. P. Kapur, E. Sanz, R. D. Palmiter, Complex I deficiency due to loss of Ndufs4 in the brain results in progressive encephalopathy resembling Leigh syndrome. *Proc. Natl. Acad. Sci. U.S.A.* **107**, 10996–11001 (2010).
73. Z. Jin, W. Wei, M. Yang, Y. Du, Y. Wan, Mitochondrial complex I activity suppresses inflammation and enhances bone resorption by shifting macrophage-osteoclast polarization. *Cell Metab.* **20**, 483–498 (2014).
74. Y. Wang, Q. Liu, T. Liu, Q. Zheng, X. Xu, X. Liu, W. Gao, Z. Li, X. Bai, Early plasma monocyte chemoattractant protein 1 predicts the development of sepsis in trauma patients: A prospective observational study. *Medicine (Baltimore)* **97**, e0356 (2018).
75. H. Matsumoto, H. Ogura, K. Shimizu, M. Ikeda, T. Hirose, H. Matsuura, S. Kang, K. Takahashi, T. Tanaka, T. Shimazu, The clinical importance of a cytokine network in the acute phase of sepsis. *Sci. Rep.* **8**, 13995 (2018).
76. A. J. Lee, B. Chen, M. V. Chew, N. G. Barra, M. M. Shenouda, T. Nham, N. van Rooijen, M. Jordana, K. L. Mossman, R. D. Schreiber, M. Mack, A. A. Ashkar, Inflammatory monocytes require type I interferon receptor signaling to activate NK cells via IL-18 during a mucosal viral infection. *J. Exp. Med.* **214**, 1153–1167 (2017).
77. M. B. Buechler, H. M. Akilesh, J. A. Hamerman, Cutting Edge: Direct sensing of TLR7 ligands and type I IFN by the common myeloid progenitor promotes mTOR/PI3K-dependent emergency myelopoiesis. *J. Immunol.* **197**, 2577–2582 (2016).
78. H. M. Akilesh, M. B. Buechler, J. M. Duggan, W. O. Hahn, B. Matta, X. Sun, G. Gessay, E. Whalen, M. Mason, S. R. Presnell, K. B. Elkon, A. Lacy-Hulbert, B. J. Barnes, M. Pepper, J. A. Hamerman, Chronic TLR7 and TLR9 signaling drives anemia via differentiation of specialized hemophagocytes. *Science* **363**, eaao5213 (2019).
79. G. L. Norddahl, C. J. Pronk, M. Wahlestedt, G. Sten, A. Ugale, M. Sigvardsson, D. Bryder, Accumulating mitochondrial DNA mutations drive premature hematopoietic aging phenotypes distinct from physiological stem cell aging. *Cell Stem Cell* **8**, 499–510 (2011).
80. K. M. Holmstrom, L. Baird, Y. Zhang, I. Hargreaves, A. Chalasani, J. M. Land, L. Stanyer, M. Yamamoto, A. T. Dinkova-Kostova, A. Y. Abramov, Nrf2 impacts cellular bioenergetics by controlling substrate availability for mitochondrial respiration. *Biol. Open* **2**, 761–770 (2013).
81. R. Erkens, C. M. Kramer, W. Lückstädt, C. Panknin, L. Krause, M. Weidenbach, J. Dirzka, T. Krenz, E. Mergia, T. Suvorava, M. Kelm, M. M. Cortese-Krott, Left ventricular diastolic dysfunction in Nrf2 knock out mice is associated with cardiac hypertrophy, decreased expression of SERCA2a, and preserved endothelial function. *Free Radic. Biol. Med.* **89**, 906–917 (2015).
82. R. K. Thimmulappa, H. Lee, T. Rangasamy, S. P. Reddy, M. Yamamoto, T. W. Kensler, S. Biswal, Nrf2 is a critical regulator of the innate immune response and survival during experimental sepsis. *J. Clin. Invest.* **116**, 984–995 (2006).
83. A. Cuadrado, A. I. Rojo, G. Wells, J. D. Hayes, S. P. Cousin, W. L. Rumsey, O. C. Attucks, S. Franklin, A.-L. Levonen, T. W. Kensler, A. T. Dinkova-Kostova, Therapeutic targeting of the NRF2 and KEAP1 partnership in chronic diseases. *Nat. Rev. Drug Discov.* **18**, 295–317 (2019).
84. J. Kwon, E. Han, C.-B. Bui, W. Shin, J. Lee, S. Lee, Y.-B. Choi, A.-H. Lee, K.-H. Lee, C. Park, M. S. Obin, S. K. Park, Y. J. Seo, G. T. Oh, H.-W. Lee, J. Shin, Assurance of mitochondrial integrity and mammalian longevity by the p62–Keap1–Nrf2–Nqo1 cascade. *EMBO Rep.* **13**, 150–156 (2012).
85. C. J. Schmidlin, M. B. Dodson, L. Madhavan, D. D. Zhang, Redox regulation by NRF2 in aging and disease. *Free Radic. Biol. Med.* **134**, 702–707 (2019).
86. N. Kubben, W. Zhang, L. Wang, T. C. Voss, J. Yang, J. Qu, G.-H. Liu, T. Misteli, Repression of the antioxidant NRF2 pathway in premature aging. *Cell* **165**, 1361–1374 (2016).
87. A. Härtlova, S. F. Erttmann, F. A. Raffi, A. M. Schmalz, U. Resch, S. Anugula, S. Lienenklaus, L. M. Nilsson, A. Kröger, J. A. Nilsson, T. Ek, S. Weiss, N. O. Gekara, DNA damage primes the type I interferon system via the cytosolic DNA sensor STING to promote anti-microbial innate immunity. *Immunity* **42**, 332–343 (2015).
88. R. Kreienkamp, S. Graziano, N. Coll-Bonfill, G. Bedia-Diaz, E. Cybulla, A. Vindigni, D. Dorsett, N. Kubben, L. F. Z. Batista, S. Gonzalo, A cell-intrinsic interferon-like response links replication stress to cellular aging caused by progerin. *Cell Rep.* **22**, 2006–2015 (2018).
89. Q. Yu, Y. V. Katlinskaya, C. J. Carbone, B. Zhao, K. V. Katlinski, H. Zheng, M. Guha, N. Li, Q. Chen, T. Yang, C. J. Lengner, R. A. Greenberg, F. B. Johnson, S. Y. Fuchs, DNA-damage-induced type I interferon promotes senescence and inhibits stem cell function. *Cell Rep.* **11**, 785–797 (2015).
90. M. F. Manchinu, C. Brancia, C. A. Caria, E. Musu, S. Porcu, M. Simbula, I. Asunis, L. Perseu, M. S. Ristaldi, Deficiency in interferon type 1 receptor improves definitive erythropoiesis in Klf1 null mice. *Cell Death Differ.* **25**, 589–599 (2018).
91. J. Finsterer, M. Frank, Haematological abnormalities in mitochondrial disorders. *Singapore Med. J.* **56**, 412–419 (2015).
92. O. Hikmat, C. Tzoulis, C. Klingenberg, M. Rasmussen, C. M. E. Tallaksen, E. Brodtkorb, T. Fiskerstrand, R. McFarland, S. Rahman, L. A. Bindoff, The presence of anaemia negatively influences survival in patients with POLG disease. *J. Inherit. Metab. Dis.* **40**, 861–866 (2017).
93. J. Van den Bossche, J. Baardman, M. P. J. de Winther, Metabolic characterization of polarized M1 and M2 bone marrow-derived macrophages using real-time extracellular flux analysis. *J. Vis. Exp.*, 53424 (2015).

Acknowledgments: We thank R. B. Mouneimne in the Texas A&M Image Analysis Lab for assistance with confocal microscopy, R. Moore for flow cytometry assistance, and H. Creed for assistance with the Vevo 3100 ultrasound. **Funding:** This research was supported by awards W81XWH-17-1-0052 and W81XWH-20-1-0150 to A.P.W. from Office of the Assistant Secretary of Defense for Health Affairs through the Peer Reviewed Medical Research Programs. Additional support was provided by NIH grants R01HL148153 to A.P.W., R01AI145287 and R01AI125512 to R.O.W., R01HL145534 to C.W.T., and NIEHS P30 ESES029067. Opinions, interpretations, conclusions, and recommendations are those of the authors and are not necessarily endorsed by the Department of Defense or NIH. **Author contributions:** A.P.W. and Y.L. designed the experiments, analyzed the data, and wrote the manuscript. Y.L. performed most of the experiments. C.G.M., S.T.-O., C.E.B., and J.D.B. assisted with animal experiments, sample processing, and/or data analyses. S.L.B. and R.O.W. contributed to the *L. monocytogenes* infections, sample collection, and data analyses. C.W.T. and L.C.W. provided expertise and advice on cardiac measurements and flow cytometric experiments, respectively. A.P.W. conceived the project and provided overall direction. **Competing interests:** The authors declare that they have no competing interests. **Data and materials availability:** All data needed to evaluate the conclusions drawn herein are present in the paper and/or the Supplementary Materials. Raw data will be provided upon request. RNA-seq datasets have been deposited in the Gene Expression Omnibus under accession number GSE171960. Additional data related to this paper may be requested from the authors.

Submitted 11 September 2020
Accepted 8 April 2021
Published 26 May 2021
10.1126/sciadv.abe7548

Citation: Y. Lei, C. Guerra Martinez, S. Torres-Odio, S. L. Bell, C. E. Birdwell, J. D. Bryant, C. W. Tong, R. O. Watson, L. C. West, A. P. West, Elevated type I interferon responses potentiate metabolic dysfunction, inflammation, and accelerated aging in mtDNA mutator mice. *Sci. Adv.* **7**, eabe7548 (2021).